UNIVERSITY OF OKLAHOMA

GRADUATE COLLEGE

SIGNATURES OF FLUID-ROCK INTERACTIONS IN THE PROXIMAL CUTLER GROUP (CO, USA) CONSTRAINED BY MINERAL CHEMISTRY AND LOW-TEMPERATURE THERMOCHRONOLOGY

A THESIS

SUBMITTED TO THE GRADUATE FACULTY

in partial fulfillment of the requirements for the

Degree of

MASTER OF SCIENCE

By

BROCK DUMONT

Norman, Oklahoma 2024

SIGNATURES OF FLUID-ROCK INTERACTIONS IN THE PROXIMAL CUTLER GROUP (CO, USA) CONSTRAINED BY MINERAL CHEMISTRY AND LOW-TEMPERATURE THERMOCHRONOLOGY

A THESIS APPROVED FOR THE

SCHOOL OF GEOSCIENCES

BY THE COMMITTEE CONSISTING OF

Dr. Andy Elwood Madden, Chair

Dr. Gilby Jepson

Dr. Gerilyn Soreghan

Acknowledgments

I would like to thank foremost Dr. Andy Elwood Madden, for your constant support and invaluable knowledge over the four years you have been my mentor. Thank you also for demonstrating the importance of expanding geosciences past the laboratory and allowing me to be a part of projects such as MinKIDS. Additionally, I would like to thank the University of Oklahoma Schultz Chair for funding support of my research endeavors.

To my committee, Dr. Gilby Jepson and Dr. Lynn Soreghan, thank you for your constructive and positive feedback throughout my project that has molded it into what it is today. Many thanks to Dr. Julian Sabisch, Dr. Preston Larson, and the rest of the Samuel Roberts Noble Microscopy Laboratory researchers, for your knowledge of theory, help with data collection, and the multitude issues and subsequent workarounds we were able to come up with. To the Structure, Tectonics, University of Oklahoma Thermochronology (STOUT) Laboratory, thank you for research support and facilities to perform in-house fission track analyses and subsequent interpretation discussions. Thank you to the University of Arizona Radiogenic Helium Dating Laboratory for zircon-helium data collection.

To my University of Oklahoma peers and friends that have supported me, the Critical Zone and Nanogeochemistry research groups, Dr. Branimir Segvic (Texas Tech University) and my friends in the office, thank you for always being open to discussion and providing feedback.

To my family, thank you for your constant motivation through the highs and lows of my academic career. You have continually pushed me towards my passions and further lit the fire underneath my feet in geosciences.

Table of Contents

List of Figures

List of Tables

Abstract

The siliciclastic Cutler Group comprises predominantly red bed strata that accumulated across large regions of the Colorado Plateau. The proximal (to the Uncompahgre Plateau) region of the Cutler Group is unique as it records subaerial exposure of complex subsurface fluid dynamics reflected in strata with either intercalated red-green and red-bleached coloration. The change from red to green or bleached colors corresponds with removal of iron oxides in bleached layers and retention of some Fe(II) in phyllosilicates and epidote in green layers, both likely through the action of one or more reactive fluid events (Hullaster et al., 2023). Permian Cutler strata onlap fractured and faulted Precambrian basement of the Uncompahgre Front, leading to a poorly constrained hydrologic system within Precambrian-hosted Unaweep Canyon. To better understand the origin and significance of color variegations in the proximal Cutler Formation, I investigated the changes in clay minerals and their associated chemistry and texture as it relates to the different colored samples. To achieve this, I integrated x-ray diffraction (XRD), scanning electron microscopy (SEM) with energy dispersive x-ray spectroscopy (EDS), with zircon (U-Th)/He (ZHe), and apatite fission-track (AFT) low-temperature thermochronology in order to provide a better separation of event(s) and a temporal framework for the greening and bleaching evident in the proximal Cutler Formation.

The data are consistent with green and bleaching alteration taking place during the Cenozoic, perhaps through the action of distinct processes related to the movement of basinal reducing fluids upwards along faults. Alteration of abundant biotite to secondary clay minerals led to distinct chemical signatures in the green and bleached layers, and red sample secondary products that overlap with both green and bleached populations. Green samples contain clays depleted in Mg, slightly enriched in Al, and with Fe preserved. Phyllosilicate alteration in bleached samples is characterized by Fe loss followed by Fe+Mg loss and Al enrichment. Interlayer K is replaced mostly with Ca in green and red samples and Na + Ca in bleached samples. The modern clay mineral alteration assemblage is consistent with the temperatures experienced by the samples post-maximum burial. Associated thermal history modelling of the AFT and ZHe data yields (1) late Jurassic-early Cretaceous maximum burial to ~150 – 200 ºC (~6 – 8 km); (2) cooling during the Eocene – Oligocene (~40 – 30 Ma) with green samples cooling to 40 ºC and 70 ºC in red); (3) beginning at ~27 Ma both samples were reheated to 80 ºC by 4 Ma; and finally (4) Pliocene (~4 Ma) rapid cooling to surface temperatures. I associate these two periods of cooling with regional exhumation associated with the Laramide uplifts and incorporation of the Colorado river headwaters, respectively. This study contributes to our understanding of the evolution of the regional fluid dynamics in the post-Permian Cutler system.

Introduction

The geologic history of the Cutler Group (hereafter, Cutler Formation) proximal to the Uncompahgre Plateau in Colorado, USA, records many signatures of tectonics, sedimentation/ erosion, and syn/post depositional fluid-rock interactions within the Paradox Basin that has resulted in variegated red, green, bleached, and drab coloration (Figure 1; Soreghan et al., 2007; Moore et al., 2008; Barton et al. 2018; Hullaster et al., 2023). These colors occur in the nominally redbed Cutler Formation proximal (within ~10 km) to the modern Uncompahgre Plateau, uplifted by basement-involved structures during Laramide deformation and more recent uplift events. The extent to which both events contributed to the modern elevation of ~2 km is still unknown (Karlstrom et al., 2012; Rønnevik et al., 2017). Bleaching within the Cutler Formation provides insight into several types of fluid-rock interactions and insight into the Paradox Basins expansive fluid-associated economic mineral deposits, hydrocarbon deposits, and bleached, former redbed sedimentary rocks (Figure 2; Barton et al., 2018).

In this study, I investigate the red/green and red/bleached interlayering in the proximal Cutler Formation to better understand the paragenesis of the modern mineral assemblages hosted within this variegated portion of the Cutler and provide additional constraints on the regional geologic history and subsurface fluid evolution. Information regarding fluid-rock interactions is recorded in the mineralogy, mineral chemistry, and texture as a function of the temperature experienced by the sediments. Previous studies of Cutler Formation bulk- and clay mineralogy found intrastratal variations throughout the Paradox Basin due to differences in depositional environment, provenance, proximity to tectonic features, and pore fluid dynamics and chemistry (e.g., Werner, 1974; Dutta and Suttner, 1986; Suttner and Dutta, 1986, Morrison and Parry, 1986; Hullaster et al, 2023).

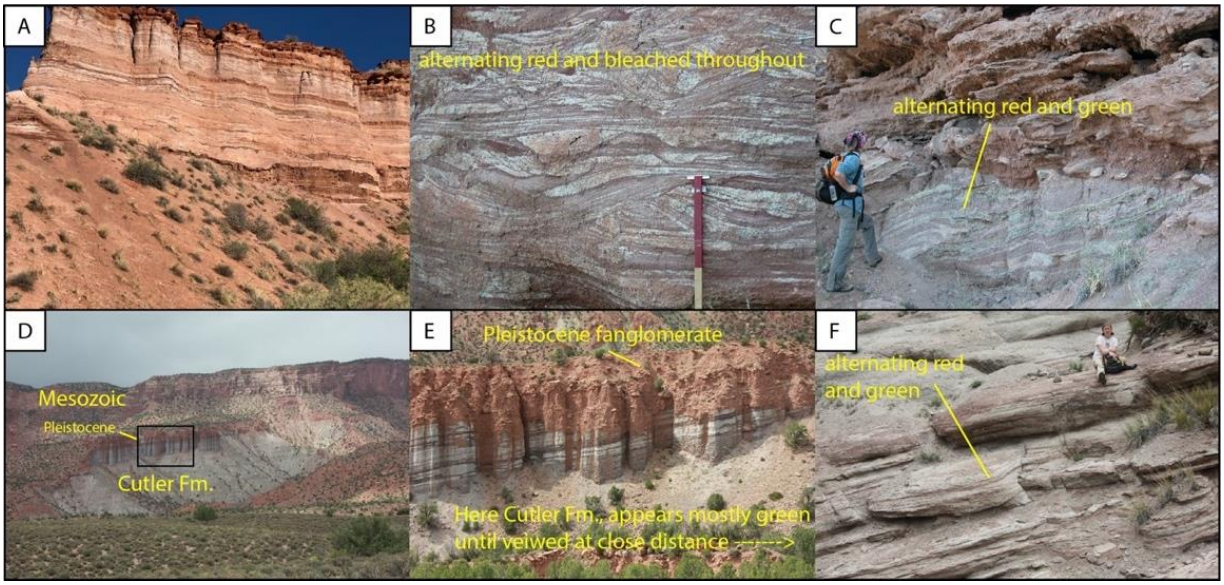

Figure 1 - Proximal Cutler Fm. field photos of outcrops demonstrating the variegated red, green, and bleached layers. (A) Red/bleached interlayering, cliff face is ~50 m high. (B) Closer view of red/bleached area; the red top of the Jacob Staff is 50 cm long. (C) Green/red Cutler underneath Pleistocene (Section V). Geoscientist is ~1.75 m tall for scale. (D) Green and red/green interlayers appear mostly green from a distance, looking north towards the location

were most. Locations of these photos can be seen in Fig. 4. Figure modified from Hullaster et al., (2023).

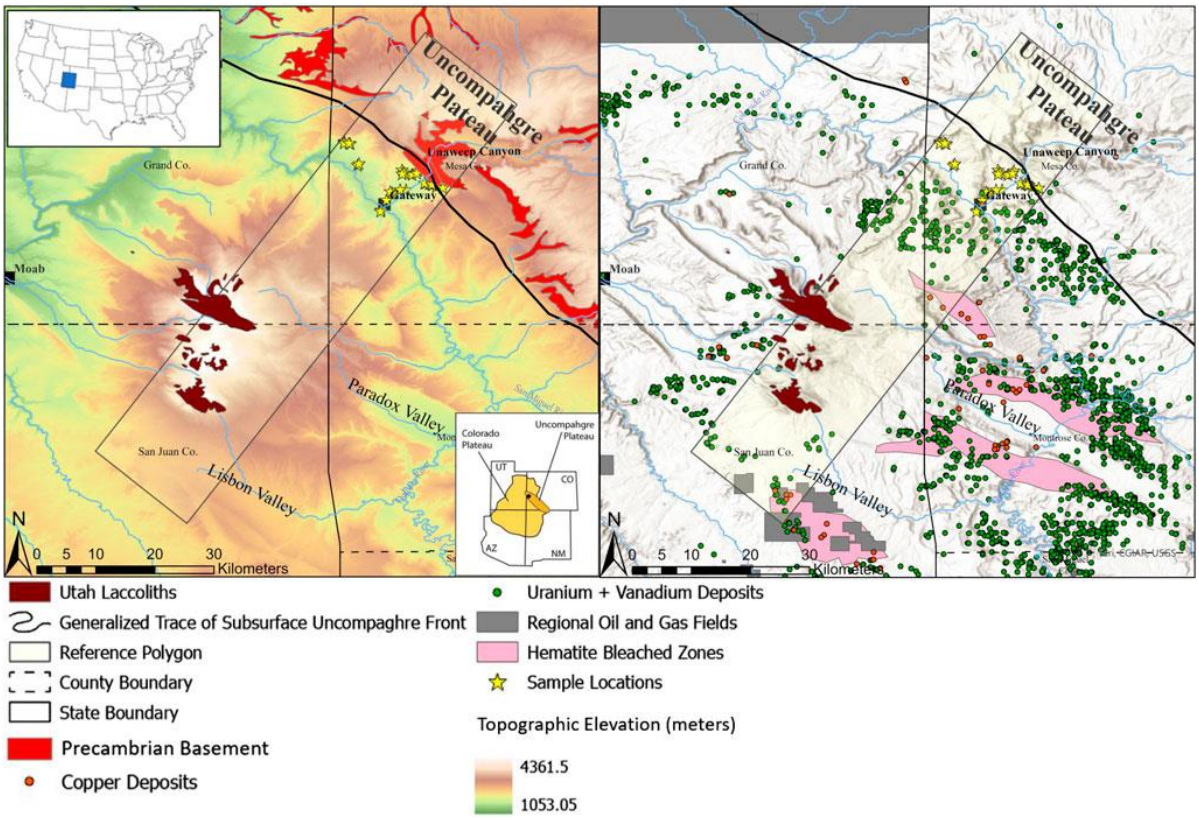

Figure 2 - Regional overview of the features of interest linked to our study area (Yellow stars), including modern topography with the Paradox and Lisbon Valleys and Unaweep Canyon (left panel), Cenozoic intrusive units (both), identified hydrocarbon, Cu, and U and V accumulations (right), estimated boundaries of extensive hematite bleaching (right), and the generalized subsurface location of the Uncompahgre Plateau bounding reverse fault. The large, shaded rectangle indicates general region of the schematic shown in Fig. 3.

The proximal Cutler Formation likely developed into a redbed during deposition or burial, with the green/red and bleached/red interlayering developing post-depositionally through contact with one or more reducing fluids (Hullaster et al., 2023). The source, and thus geochemistry, of the reduced fluids needs to be explored in order to understand the chemical influence they will likely have on authigenic clay minerals. The migration of these fluids are just as pertinent and depends on the climatic, sedimentary, and tectonic frameworks present in order to be able to propagate these fluids through the subsurface (Fig. 3, Barton et al., 2018). Within the proximal Cutler Formation, there is a correlation between grain size and coloration, decreasing from bleached to green to red units. Hullaster et al. (2023) characterized samples with similar biotite concentrations from both green- and red-colored samples and found individual grains to be ~1000 µm and ~150 µm, respectively. These coarser grained green and bleached intervals are suggested to provide a preferential pathway for any of the various fluids to propagate, leaving relatively undisturbed redbed strata.

Potential sources of reducing fluids include (Fig. 3B): (1) Meteoric groundwaters flowing downgradient from the uplifted Uncompaghre Plateau, concentrated along the contact between Precambrian basement and Cutler strata (Soreghan et al., 2007, 2009, 2014; Barton et al., 2018). (2) Hydrothermal fluids mobilized due to igneous activity associated with the emplacement of the nearby La Sal Laccolith. Emplacement of laccolithic units (La Sal, Henry, and Abajo Mountains) in the Paradox Basin facilitated subsurface flow of thermally influenced magmatic fluids in the Oligocene (~30 Ma) associated with bleaching events in the Lisbon Valley (Reynolds et al., 1985; Murray et al., 2016, 2019). (3) Deep basinal fluids rising upwards along faults and contacts. Sandstone bleaching events in the Paradox Basin have been linked geochemically to Cu mineralization and migration of mature petroleum-related fluids along faults and fractures, from late Cretaceous to Eocene time (Nuccio and Condon, 1996; Kim et al., 2022; Bailey et al., 2023). Additionally, the Cenozoic topographic and erosional evolution of the Colorado has been suggested as a possible mechanism for bringing deep brines such as saline waters from dissolution of the older evaporitic deposits of the Hermosa Formation towards the surface (Murray et al., 2016; Barton et al., 2018; Murray et al., 2019; Kim et al., 2022; Bailey et al., 2023).

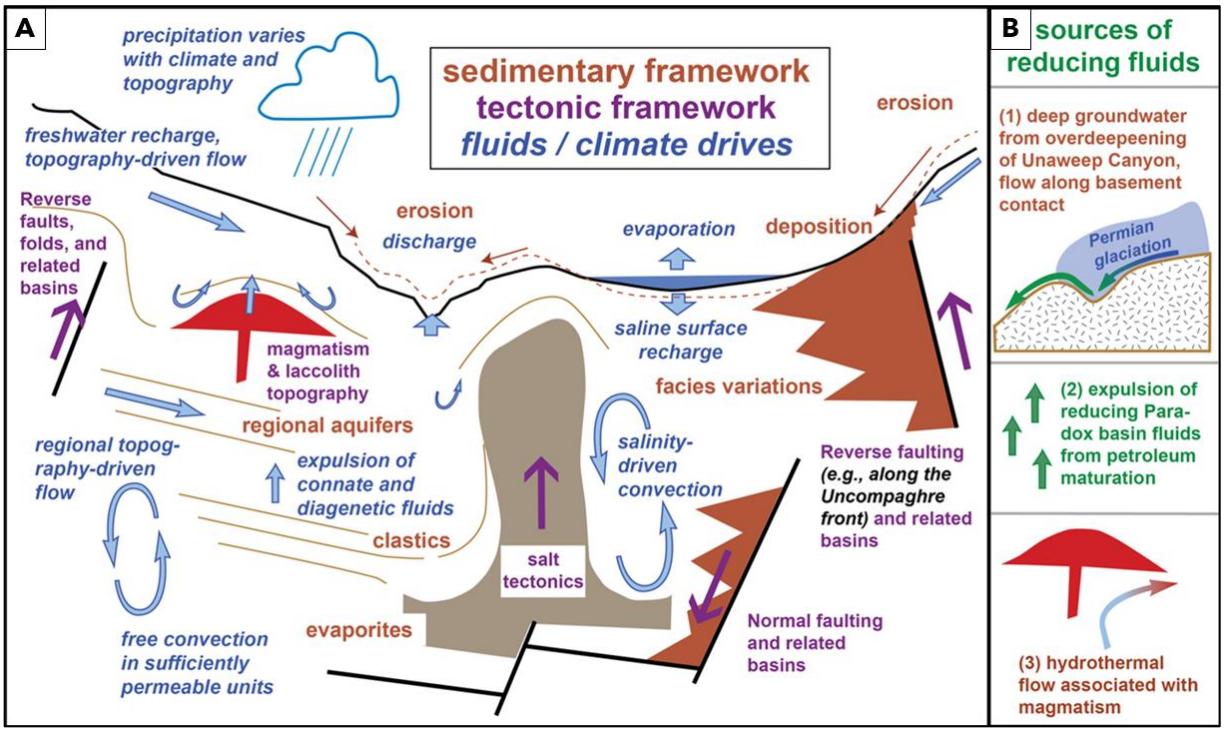

Figure 3 - Generalized schematic cross section illustrating the sedimentary and tectonic framework in the Paradox basin region, along with fluid flows, adapted from Barton et al. (2018). This study area lies along a basin-bounding uplift, such as the major reverse fault to the right-hand side. The right-hand panel illustrates three sources of reducing fluids that may have contributed to alteration of the proximal Cutler.

Iron has been suggested as a major control on the red-green-bleached coloration in sedimentary rocks based on valence state and coordination/mineralogy (Keller, 1953; Van Houten, 1973; McBride, 1974). Compared with the more distal Cutler Formation, which contains iron predominantly in iron (III) oxides (Reynolds, 1985), biotite and epidote comprise a large fraction

of the detrital iron proximal to the Uncompahgre Front and provide an important starting point for investigating clay and Fe-bearing mineral authigenesis and recording fluid-rock interactions. Biotite weathering proceeds differently under different redox conditions and temperatures (e.g., Hoffman and Hower, 1979; Banfield and Eggleton, 1988; Claeys and Mount, 1991; Jiang and Peacor, 1994; Murakami et al., 2004; Parneix et al., 1995; Sugimori et al., 2008). Secondary clay minerals, such as chlorite and mixed-layer chlorite-smectites, record the chemistry and temperature of their formation (e.g., Bettison-Varga et al., 1991; Lanari et al., 2014; Beaufort et al., 2015; Inoue et al. 2018; Pant et al., 2019) and are often associated with green colors of sedimentary rocks (Wu et al., 2019) due to the incorporation of reduced ferrous iron accumulating in the clay structure. Reducing fluids will also facilitate mineralization of other metals, such as Cu and U (e.g., Wu et al., 2019), which are more mobile under oxidizing conditions and accumulate in contact with reducing agents in fluids or sediments contained within the Paradox Basin (Reynolds, 1985; Barton et al., 2018; Kim et al., 2022; Bailey et al., 2023). As mentioned, clay authigenesis depends on formation conditions (i.e. water and rock chemistry, oxidation conditions, and temperature); therefore, the temperatures and timing of heating and cooling of the proximal Cutler Formation will provide the final constraint to understand the paragenesis of the modern mineral assemblage.

The origin of bleaching and greening in the proximal Cutler region could reflect: 1) burial and hydrocarbon influence, similar to other regions of the Colorado Plateau, 2) a reducing fluid event such as hydrothermal alteration from magma emplacement following maximum burial, or 3) an unknown or combination of mentioned events. Unraveling this will provide insight into the paragenesis of the green and bleached units as a single system or distinct events as it relates to the original redbed geology. In this work, I apply clay mineralogy/geochemistry and low-temperature thermochronology to provide detailed constraints on the greening and bleaching events as they relate to fluid chemistry and temperatures of alteration. I integrate my results with published data to constrain possible mechanisms for bleaching and greening. This work provides insights on subsurface fluid-flow and mineralization within the Paradox Basin, specifically near the Uncompahgre Plateau.

Geologic Context

The Paradox Basin is a sedimentary basin spanning parts of Colorado, Utah, New Mexico, and Arizona, U.S.A (Figure 2). Within the Paradox Basin, deposition of the proximal Cutler Formation occurred as Ancestral Rocky Mountain (ARM) orogenesis initiated in the Pennsylvanian and continued through the Permian (Sweet and Soreghan, 2010; Soreghan et al., 2012; Leary et al., 2017). This deformation took place in an intraplate setting encompassing much of western/midcontinent North America and consisted of northwest-trending, basement-cored uplifts (Sweet and Soreghan, 2010: Fig. 1) and associated sedimentary basins (Kluth and Coney, 1981; Sweet and Soreghan, 2010). The Uncompahgre Uplift is one of these block uplifts, bounded by a buried reverse fault(s) on the southwest (Uncompahgre front), and was the source for Cutler deposition proximally (Moore et al. 2008). The initial exhumation of the Uncompahgre Uplift occurred in the Pennsylvanian-Permian in response to deformation associated with the ARM orogeny (Soreghan et al., 2015). Sedimentation during the Mesozoic comprised largely marine units (e.g. the Mancos Shale and Morrison Formation) that extend across the Uncompahgre Plateau and bury the Cutler Formation distally but have been eroded above the proximal part of the Cutler Formation.

During the Late Jurassic, subduction of the Farallon plate began along the western North American passive margin (e.g., DeCelles, 2004). Oceanic plate subduction was associated with the development of an extensive magmatic arc (Copeland et al., 2017) and fold and thrust belt to the west of the study region (Decelles, 2004). By the late Cretaceous, the Farallon slab transitioned to subhorizontal subduction, evidenced by shift in the magmatic front far into the North American hinterland (DeCelles, 2004; Copeland et al., 2017). Flattening of the Farallon slab is associated with a change in structural style to thick-skinned, basement-involved deformation (e.g. Erslev, 1991). These structures occur throughout the Colorado Plateau and are known as "Laramide uplifts" (e.g. Yonkee and Weil, 2015). Laramide uplifts such as the White Mountain Uplift in the northwest Colorado Plateau document an early Paleogene (~58 – 53 Ma) timing of exhumation (Naeser et al., 2002). Flat-slab (subhorizontal) deformation persisted until ~50 Ma, at which the slab began to founder and roll-back (Copeland et al., 2017, Decelles, 2004, Dickinson and Snyder, 1978). The Farallon slab rollback is associated with a magmatic flare up in the region from Eocene to Miocene (~49-18 Ma) which overlaps temporally laccolithic emplacement of the La Sal, Henry, and Abajo mountains. The La Sal laccolith is the most proximal magmatic unit to the southwest of this study region (~50 km) with a crystallization age of 29.1 ± 0.3 Ma (Rønnevik et al., 2017). Following Oligocene emplacement of laccolithic bodies, periods of limited erosion in the Miocene and subsequent rapid Pliocene exhumation around 4 Ma leading to shifts in regional groundwater flow (Murray et al., 2016; Rønnevik et al., 2017; Murray et al., 2019; Bailey et al., 2023). Uplift and exhumation of the Colorado Plateau in the more recent Miocene (~6 Ma) time has been suggested as a contributing fctor to groundwater circulation (Bailey et al., 2023).

Distinct lateral and vertical changes in facies and depositional systems have led to debated climatic conditions during deposition. Environmental interpretations range among fluvial, eolian, and marine in the distal regions (Condon, 1997) and lacustrine and fluvial-alluvial proximal to the Pennsylvanian-Permian Uncompahgre Uplift (Werner, 1974; Dutta and Suttner, 1986, Soreghan et al., 2007). The proximal Cutler Formation overlies the evaporitic Paradox and Honaker Trail formations and accumulated during active salt movement, which can be seen in interbedded salt and lower Cutler beds (White and Jacobson, 1983). White and Jacobson (1983) propose ~4.2 – 7.9 km of displacement along the Uncompahgre Front and the created accommodation space generated from the displacement allowed for Cutler sediments to be deposited before depositionally onlapping the uplift from which is was sourced (Fig. 3; Condon, 1997; Soreghan et al., 2007, 2009). In this study area proximal to the Uncompahgre Front, the sediments are arkosic and sourced from 1.6 - 1.4 Ga alkali feldspar granite, monzogranite, and related metamorphic basement exposed in the Uncompahgre Uplift (Case, 1991). Outside the study region (>15 km from the front), within the Paradox Basin, Cutler sediments include contributions from Appalachian orogenic sources (e.g., Lawton et al., 2021). The estimated total thickness of the Mesozoic strata preserved in the Book Cliffs is ~2 – 3 km (Gualtieri, 1988 and Rønnevik et al., 2017) but has been removed in the proximal most portion of the Cutler formation where this study is focused.

Methods

Sample Collection

The specimens utilized in this study had been previously collected by Soreghan et al. (2007) and Hullaster et al. (2023). Specific collection methods are described in more detail there, and Fig. 4 illustrates the distribution, nomenclature, and coloration of samples. Thermochronological and clay mineral analyses in this study utilized sedimentary rock samples to constrain burial and paleotemperature evolutions. In order to resolve possible temperature variations between green and red Cutler rocks, proximal green (1218-03) and distal red (63S-XII-37.5) samples were selected for apatite fission-track and zircon (U-Th)/He analyses. Apatite, zircon, and epidote grains were separated from each sample following standard mineral separation procedures.

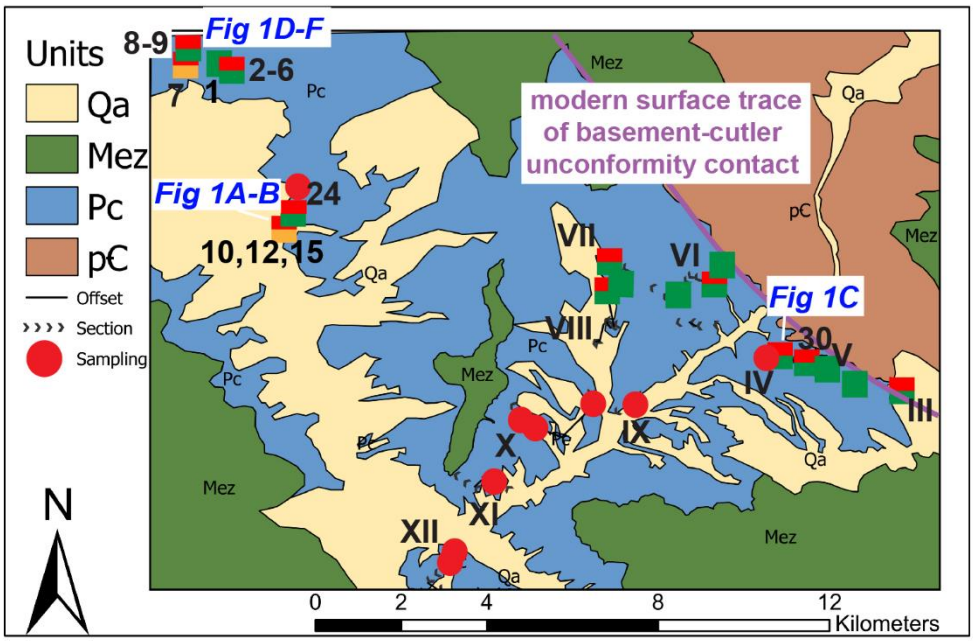

Figure 4 – Study region sample locations (stars in Fig. 2) with the color of the polygon at the sample site demonstrating the colors of the rocks. The rocks pictured in Fig. 1 are also depicted here spatially with respect to the Uncompahgre Plateau. Geologic units visible include Precambrian Basement (pЄ), Permian Cutler Formation (Pc), and Mesozoic (Mez) and Quaternary (Qa) deposits have been grouped. Samples with a single number correspond to samples with a "1218" notation in Table 1. Figure modified after Hullaster et al. (2023)

Table 1 – Overview of samples including latitude and longitude (from field measurements), elevation values from Google Earth according to the lat./long. values, and lithology. More in-depth description of lithology is given in the text and included here using notation of facies from Soreghan et al. (2009). Methods include powder random X-ray diffraction (RXRD) measurements of the extracted <2 μm (clay) grain size fraction, optical petrography (Pet) of whole rock thin sections focusing on biotite alteration, scanning electron microscopy with energy dispersive spectroscopy (SEM-EDS) of uncovered and coated thin sections for imaging

and chemical analysis, and apatite fission track (AFT) and zircon (U-Th)/He (ZHe) for thermal modeling for proximal Cutler sediments.

Sample	Lat	Long	Elevation (m)	Lithology	Methods
1218-03 Green	38.774957	-109.027070	1,566	Sandstone	RXRD, Pet, SEM-EDS, AFT, ZHe
1218-04 Red	38.774957	-109.027070	1,566	Granule conglomerate	RXRD
1218-07 Bleach	38.776065	-109.036520	1,529	Sandstone	RXRD
1218-15 Red	38.744646	-109.013740	1,449	Granule conglomerate	RXRD, Pet, SEM-EDS
1218-15 Bleach	38.744646	-109.013740	1,449	Granule conglomerate	RXRD, Pet, SEM-EDS
1218-30 Green	38.714481	-108.904260	1,621	Sandstone	RXRD, Pet
1218-30 Red	38.714481	-108.904260	1,621	Granule conglomerate	RXRD
1218-30 Black	38.714481	-108.904260	1,621	Sandstone	RXRD
53 III 14C Green	38.708000	-108.886000	1,775	Granule conglomerate	Pet, SEM-EDS
53S IV 230 Green	38.715000	-108.912000	1,567	Granule conglomerate	RXRD
53S IV 244.5 Red	38.715000	-108.914000	1,576	Pebble diamictite	RXRD, Pet, SEM-EDS
63S VIII 47 Green	38.729000	-108.948000	1,629	Granule conglomerate	RXRD
63S VIII 47 Red	38.729000	-108.948000	1,629	Granule conglomerate	RXRD
63S XII 16.5 Red	38.674000	-108.980000	1,401	Granule conglomerate	RXRD, Pet
63S XII 37.5 Red	38.672000	-108.981000	1,408	Sandstone	RXRD, Pet, AFT, ZHe

Clay Fraction Separation

Using the methods described by Moore and Reynolds (1997), clay grain-size fractions were separated from whole rock samples. Rocks were initially crushed using a percussion mortar and passed through a 0.4 mm sieve. 1-3 g of material were sieved due to varying quantities of clay minerals present in the different colored samples. Sodium hexametaphosphate (as a dispersant) is added to the sieved fraction and combined with 150 mL of distilled water before ultrasonicating. Ultrasonication is done in 10 second increments followed by 10 seconds of rest for 10 minutes total. This step is followed by centrifugation at 800 rpm for 4 minutes. The supernatant is

decanted from the settled sediment and filtered using a Millipore filter or dried in the oven at 50 °C until the solution is removed and only the clay fraction (2 micron) remains for analysis.

Scanning Electron Microscopy

Uncovered thin sections were analyzed via SEM to observe chemical variations among the alteration products of biotite within the different-colored sections. Epidote grains were mounted and embedded in epoxy, ground and polished to reveal grains, and placed on a grid holder for analysis in hopes of elucidating any growth or chemical variations correlating to formation conditions. SEM data was collected on the ThermoFisher Quattro S FE-ESEM at the University of Oklahoma's Samuel Robert Noble Microscopy Laboratory. Images were collected at 20 kV using SE and BSE detectors. Chemical data was collected using a 30 mm^2 UltraDry EDS system.

The ThermoFisher Pathfinder software was used to automate collection of large-area datasets as well as chemical mapping within both biotite and epidote. High-resolution EDS maps were completed to visualize the spatial distribution of chemical variations with respect to textures and secondary products. From these maps, individual data points were selected from areas of interest for further quantification and interpretation. The atomic percentages obtained via SEM-EDS from 27 biotite grains were analyzed and plotted as 77 data points representative of unaltered to highly altered biotites from rocks of each color (red, green, bleach). These data are plotted as ternary diagrams of the atomic percentages of octahedral and interlayer cations scaled to their proportions out of 100% in each grain to analyze biotite alteration trends within the clay structure.

Powder X-ray Diffraction (XRD)

Clay size fraction extractions were performed on selected whole rock samples and analyzed by X-ray diffraction to understand their mineralogy and octahedral sheet character. All XRD analyses were done using a Rigaku SmartLab X-ray diffractometer using Cu-Kα radiation with a voltage of 45kV, 200 mA of current, a pre-sample multilayer mirror to suppress Kβ contributions, and a Hypix 3000 direct counting detector. The collected spectra were imported into Jade Pro linked to the ICDD-PDF4+ database for interpretation. For the clay fraction random mount XRD analysis performed in this study, data collection occurred over a 2Θ range of 5-65 degrees at a scan rate of 10°/min with secondary scans of the (060) area at 1°/min .

Apatite Fission-Track Analysis

The fission-track thermochronometers rely on the spontaneous fission decay of ^{238}U (Hurford and Green, 1983; Jepson et al., 2021) which causes damage "tracks" in the mineral lattice. Within apatite, these tracks are annealed instantaneously on geologic timescales at temperatures above the apatite partial annealing zone (~120 - 60 °C) making it a powerful tool for constraining upper-crustal cooling (Braun et al., 2006; Green et al., 1986, Gallagher et al., 1998). Apatite fission-track analyses (AFT) were performed at the Structure, Tectonics, University of Oklahoma Thermochronology (STOUT) Laboratory. Apatite grains were mounted in epoxy and polished to expose internal surfaces before spontaneous fission-tracks are revealed through etching with 5.5M nitric acid for 20 ± 0.5 seconds at 20 ± 1°C. Apatite fission track density, lengths, and etch pits were counted and measured using a Zeiss AxioImager2 microscope and Fijjiontrack plugin (Lang et al., 2023) within Fiji ImageJ. Confined fission track length distributions were measured to determine cooling rates from mean track lengths (MTL).

Distribution of these measured confined track lengths give insight into the residence time within the apatite partial annealing zone (APAZ) with shorter MTLs indicating extended exposure to APAZ temperatures (Laslett et al., 1982). The concentration of ^{238}U in the counted areas of apatite was determined using laser ablation inductively coupled plasma mass spectrometry (LA-ICP-MS). Age calculation was carried out using in-house R script following equations as described in Hasebe et al. (2004) and Vermeesch (2017), using the Durango apatite (McDowell et al. 2005) to perform a session-zeta calibration (Vermeesch 2017).

Zircon (U-Th)/ He Analysis

The (U-Th)/He thermochronometer relies on the accumulation and thermally activated diffusion of radiogenic ^{4}He (Flowers et al., 2020). The closure temperature for zircon (U-Th)/He (ZHe) is below ~180°C, thus it is valuable for determining middle- to upper-crustal cooling (Reiners, 2005) especially when integrated with other low-temperature thermochronological methods. Zircon analyses were completed at the Arizona Radiogenic Helium Dating Laboratory at the University of Arizona and followed the protocols described in Reiners (2005). Helium (^{4}He) was extracted at 900°C–1300°C, under ultra-high vacuum with a diode laser and measured via isotope dilution on an Element 2 mass spectrometer at the University of Arizona. Following ^{4}He extraction, tubes which contained zircon were retrieved from the laser cell, then spiked with ^{235}U and ^{230}Th and dissolved. Blank, Sample, as well as spiked standard solutions were subsequently analyzed via isotope dilution for ^{238}U and ^{232}Th via ICP-MS (Reiners, 2005). Replicate analyses Fish Canyon Tuff zircon were used as an internal standard (n = 2) yielded a mean (U-Th)/He age of 28.4 ± 0.8 Ma (1σ), consistent with the Fish Canyon Tuff (U-Th)/He reference age of 28.3 ± 0.8 Ma (Gleadow et al., 2015).

Thermal History Modeling

Thermal history modeling was performed on both samples (proximal 1218-03 green and distal XII 37.5 red) using AFT (MTL and single-grain ages) with Dpar (e.g., Donelick et al., 2005) used as a kinetic parameter and single grain ZHe data. The QTQt software (version 5.7.1) was used to determine the thermal history. The QTQt software applies a Bayesian trans-dimensional approach to Markov Chain Monte Carlo statistics (Gallagher, 2012) to produce a cooling evolution of the sample that predicts the measured data by applying the AFT annealing model after Ketcham et al. (2007) and the ZHe radiation damage model after Guenthner et al., (2013). In our approach we used an initial unconstrained run to explore the statistical space, that was then followed by adjustments to the search parameters as well as the addition of geological constraints. A large number of iterations (>>100,000) were run as to generate a range of models that can constrain a probability distribution. From the obtained probability distribution an individual thermal history can be selected, such as the maximum likelihood as well as an "expected" (weighted mean) paths.

Results

Mineral Texture and Chemistry as Evidence for Fluid-Rock Interaction

Petrography

Petrographic analyses of red, green, and bleached samples focused on biotite alteration as signatures of fluid-rock interaction. The optical characteristics of the altered biotites were

investigated at a macroscopic scale with petrography before a higher resolution investigation into the grains take place to correlate small-scale mechanisms with macro scale grain texture.

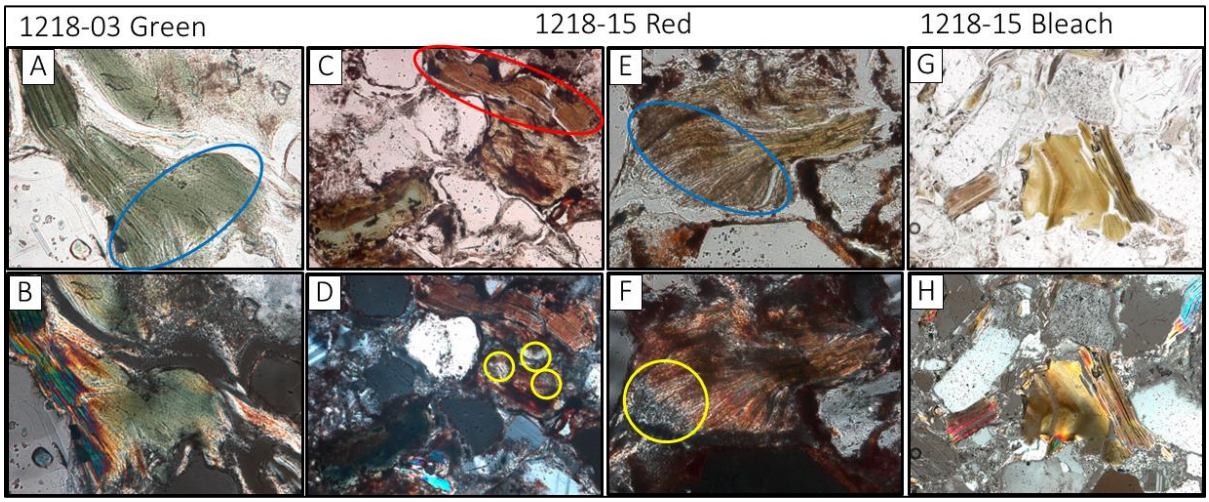

Figure 5 –Photomicrographs of biotites from green, red, and bleached samples, in both plane-polarized light (upper row) and the corresponding region in cross-polarized light (bottom row). These images show examples of common biotite textures such as relatively pristine grains (C, red oval), often bent due to compaction (A,B,G,H), oxidation that follows intergranular fractures or along layers (C-F), patchy oxidation (C,D), chloritization (A-D), edge alteration (A,B,E,F, blue oval) and volume expansion (A,B,E-H), replacement or transformation to high-birefringence clay (A,B), and near complete replacement by iron oxides and low birefringence clays (C,D, yellow circles).

Euhedral, brown-tan pleochroic biotite occurs in all samples regardless of RGB color with secondary products including opaque Fe-Ti oxides, quartz, chlorite, and other clays indistinguishable at this scale (Werner, 1974). Example, relatively pristine, biotite can be seen in Fig. 5C (red oval) as slightly bent and oxidized with little secondary mineralization taking place. This is the idealized starting point of an inherited biotite undergoing little to no alteration and used to interpret the textures and chemical variations among the remaining color sections.

Red-sample biotites exhibited the largest variety of alteration textures from unaltered to highly altered. These grains tend to exhibit pervasive hematization (Fig. 5C-F) compared to the other samples, although green and bleached samples still retain evidence of oxidative hematization as grain dustings (Fig. 5G, H). Intergranular fractures and along cleavage planes are extensively hematized in red grains with some grains exhibiting a patchy oxidation texture with alteration to lower birefringent clays (Fig. 5C, D, F). Edge alteration, a common biotite alteration texture, is also evident in these red samples with the secondary products again consisting of low birefringent clays.

Contrary to the red samples, the biotites in the green and bleached samples contain extensive secondary chloritization along cleavage planes (Fig. 5A, B) and complete pseudomorphic replacement in some bleached grains (Fig. 5G, H). Within the green grains exhibiting this edge alteration, chloritization occurs as opposed to replacement with the low birefringent clays as in the red samples. This chloritization into the grain is accompanied by a volume increase

contributing to the alteration texture (Fig. 5A, B, G, H). The pseudomorphic replacement rather than edge alteration leads to a slightly different texture in which bleached grains experience the volume increase but from the interior of the grain propagating outwards leading to a whole grain folding texture (Fig. 5G, H). The oxidation in red samples has been stripped away, outside of some dusting (e.g. Fig. 5G/H). Opaque minerals preserve transformation of layers propagating through entire cleavage planes in bleached grains (Fig. 5G, H) and has been noted as an alteration product for extensive biotite alteration at the micro-/nanoscale (Wu et al., 2019) and observed macroscopically here.

Electron Microscopy

In order to evaluate the chemical fingerprint of fluid-rock interactions, we present data on chemical variations among biotite grains and their direct alteration products using SEM-EDS. Since the biotite grains are primarily reacting to form other phyllosilicates (along with Fe-Ti oxides), we use ternary plots representing cations commonly found as the major component of phyllosilicate octahedral sheets (Fig. 6, left) and interlayers (Fig. 6, right) to demonstrate trends from less-altered biotite cores to surrounding reaction products. Polygons, chosen by inspection, are used to depict groupings of similar chemistries often correlatable to a single color (red, green, bleached) and arrows represent evolution from a more unaltered detrital core to an altered edge/pore within a single grain. 4 data points (Fig. 6, stars) from the red samples come from a ~100 µm thick unaltered biotite and a lithic fragment and are presented as the bottom threshold/starting point of subsequent clay authigenesis (Figure 6 and 7). Further analysis of variability in the red, green, and bleached samples will be described with respect to these starting chemistries. Additionally, compositions of Clay Minerals Society standard /special clays are included for context (Kogel, 2001 and Mermut, 2001).

In general, all samples show conservation or enrichment of Al and depletion of K relative to many of the unaltered biotite grains (Fig. 6, left, stars), plotting on the upper half of the ‘octahedral’ ternary. Several (9 out of 77) points plot coincident with the unaltered biotite at >95% K in the ‘interlayer’ ternary (Fig. 6, right) and cannot be clearly seen, but a majority of the points demonstrate loss of K and addition of Ca and/or Na. However, beyond these generalizations, the data separate into distinct chemical signatures of alteration.

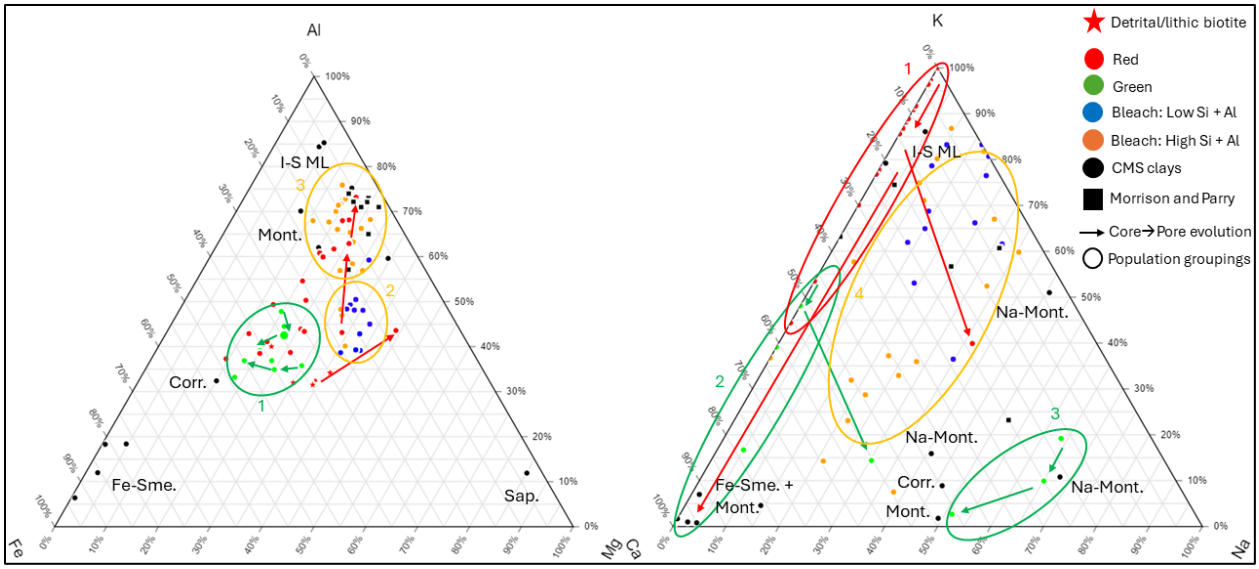

Figure 6 – (left) octahedral chemistry ternary (right) interlayer chemistry ternary. The values are scaled to their respective proportions out of 100% and can be seen by the values on the fringe of the plot. Red and green dots represent individual data points sampled from an altered biotite from the respective colored sample. Yellow and blue dots represent data points taken from altered biotites from bleached samples. Arrows represent an alteration sequence from a core of a grain to an adjacent area of authigenic clay mineralization. Arrows are absent in bleached samples due to the dominance of layer transformation textures rather than progressive alteration from the core to edge of grains as observed in red and green samples. Black circles illustrate compositions of Clay Minerals Society standard clays (Kogel, 2001 and Mermut, 2001). Black squares represent the chemistry of clays reported in the literature for Cutler Formation bleached grains (Morrison and Parry, 1986). Populations (discussed in text) are numbered and grouped according to color and chemical trend. See text for more details.

Considering the octahedral cation ternary (Fig. 6, left), there are three populations distinct from the original unaltered biotite that correlate with the color of the rock they were taken from: one encompassing all green samples (population 1, green points, Fig. 6, left) and two populations of bleached biotites (population 2 and 3, blue and yellow points, Fig. 6, left). There is no clear population of red samples; instead, they overlap with all three of the aforementioned populations in both chemistry (red points, Fig. 6, left) and texture (Fig. 7).

Biotites from bleached rocks commonly exhibit deformation due to compaction and/or alteration causing structural deformation (Figure 7K-M). At the petrographic and SEM scales, they typically exhibit a high degree of layer transformation, with alteration products in layers interspersed between what appear to be less-altered layers (Fig. 7K-M). SEM-EDS analyses of these morphologically distinct regions demonstrate two populations of compositions that are distinct from the original biotite and from each other (Fig. 6, blue and yellow circles, labeled with a '2' and '3' respectively). The distinction among the two bleached populations is degree to which iron and magnesium have been removed, with mostly Fe>>Mg removal in the population represented by the blue points (2) and Mg+Fe removal and the highest aluminum enrichment represented by the yellow points (3). Compared to biotite, the green samples maintain similar iron concentrations with slight Mg loss and Al enrichment. The observed morphological features

of the green biotites are dominated by an edge opening alteration propagating inward and secondary mineralization in adjacent pore spaces rather than neoformation of original biotite layers (Fig. 7F-J). When observing trends from the core of green biotite grains to secondary clay products in adjacent areas, both analyzed progressions demonstrated similar shifts towards CMS clay mineral standard for trioctahedral corrensite (CorWa-1) (Fig. 6).

Considering cations commonly associated only with the phyllosilicate interlayer (Figure 6, right), chemical analyses are grouped into four dominant populations. Red sample biotites are generally less altered, with higher potassium content in the interlayer and in some cases a progression of potassium replacement with calcium (population 1). This is the same population of red grains that demonstrated the large variability within the octahedral sheet (Fig. 6, left). Population 2 consists of the majority of green analysis points and demonstrates a similar trend of calcium replacement of potassium but to a greater degree than population 1. Population 3 consists of 3 spots analyzed from a line starting in a green altered biotite and progressing into the secondary products at the grain edge/adjacent pore space. The initial analysis point has low potassium (18%) and very high sodium (64%) concentrations and undergoes further potassium loss and calcium-for-sodium replacement, ending very close to a CMS clay mineral standard for montmorillonite (Otay-SCa-3) and/or corrensite (CorWa-1). The final grouping (4) consists of most of the analysis points from bleached samples and has more sodium incorporated into the interlayer than populations 1 and 2 (red and most green) but demonstrates a similar potassium replacement with calcium while maintaining its Na concentration. Population 3, the remainder of green points not in population 2, has the highest sodium concentration but demonstrates a calcic replacement of both sodium and potassium.

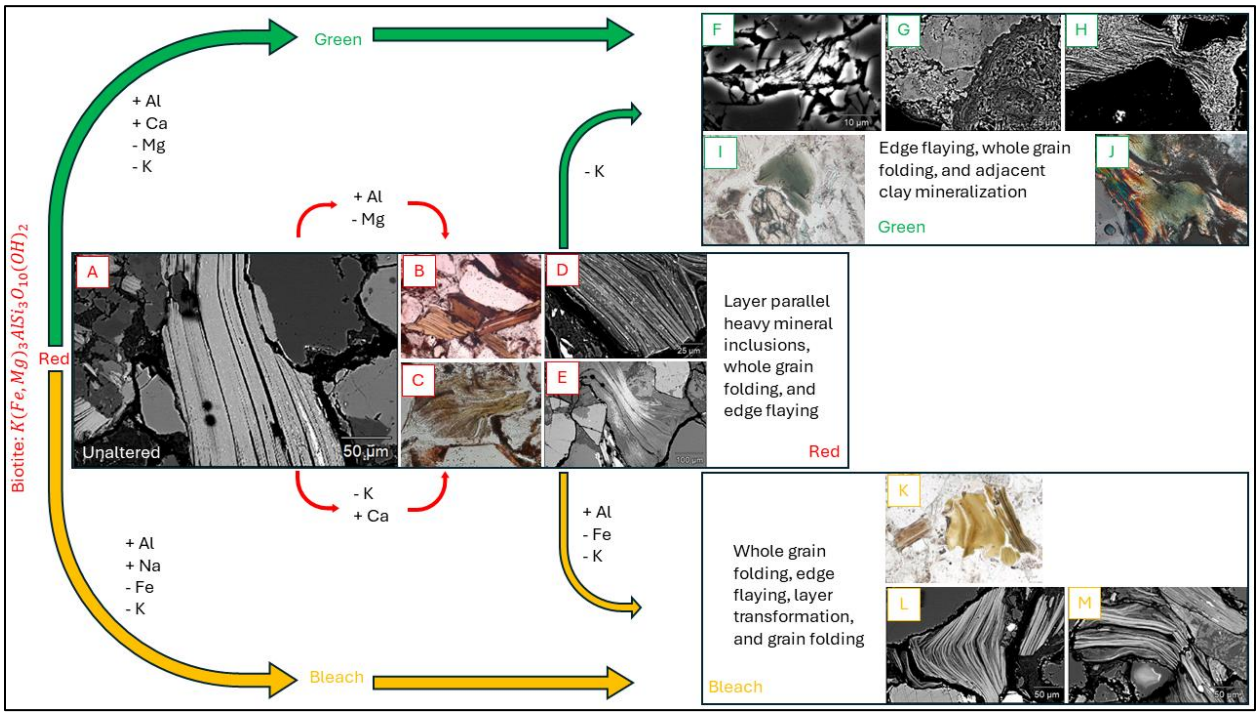

Figure 7 – Correlation diagram among the biotite alteration occurring in the various RGB color sections. Chemistry and micro-/macrotextures are depicted. Layer parallel heavy mineral inclusions include apatite, titanite, and Fe/Ti- oxides. The ideal biotite chemical formula is

provided as a reference point for alteration. Note that in the red layers, some iron is present as Fe^{+3} in ferric oxides such as hematite and Fe-Ti oxides associated with altered layers the biotite.

Populations of analysis points that group together in the octahedral ternary also group together based on interlayer cation chemistry, apart from an extra population of green samples (4) in the interlayer ternary (Fig. 6). This extra population coincides with extremely altered biotites and a pore region (Figure 7G) and plots near the CMS special clay formula for corrensite in the octahedral ternary and sodium montmorillonite/corrensite in the interlayer ternary. Looking at the various populations with respect to the initial biotite (Figure 6, stars) apparent reaction pathways can be interpreted among the samples from the differently colored rock layers with the goal of delineating them as multiple alteration events of varying conditions or one event that redistributed system elements among the colors differently. The arrows of Fig. 6 show the evolution from the core of a biotite to the more altered edges and adjacent pore space (when applicable), providing a microsystem view of potential reaction pathways. Generally, these microsystems mirror the overall compositional evolution described for the populations above for the typical octahedral sheet cations. Interestingly, one red microsystem (Fig. 6, left, lower red arrow) shows a core composition nearly identical to ideal biotite, with Fe loss and Mg/Al conservation in the alteration products. This microsystem can be seen correlating to the red arrow on the left axis on the interlayer ternary demonstrating full replacement of interlayer potassium with calcium (Fig. 6, right). The two trends among bleached grains and previously discussed are also highlighted by two red microsystem evolutions (Fig. 6, left). For the interlayer cations, two of the reported red microsystems showed the reported calcium-for-potassium trend. However, one red microsystem and one green microsystem showed a majority Na>>Ca replacement of K (Fig. 6, right). Morrison and Parry (1986) observed clays, near bleaching events at Lisbon valley, which have been plotted here (Fig. 6, black squares). The green grains show a separate trend of alteration that is complimented by variations in interlayer chemistry, highlighted by population 3 (Fig. 6, right).

Clay Fraction Octahedral Sheet Chemistry via X-Ray Diffraction

Phyllosilicate octahedral sheet chemistry is revealed via random mount x-ray diffraction (XRD) analyses of clay *b*-dimensions in this study and further confirmed with SEM-EDS results. However, random orientation XRD of the clay fraction is not easily interpretable without an understanding of the clays present, which was previously determined for proximal Cutler samples by Hullaster et al. (2023) by air-dried, glycolated, and heat-treatment XRD analysis of oriented samples. They identified smectite, illite, chlorite, and chlorite-smectite and illite-smectite mixed layer clay minerals (Hullaster et al., 2023).

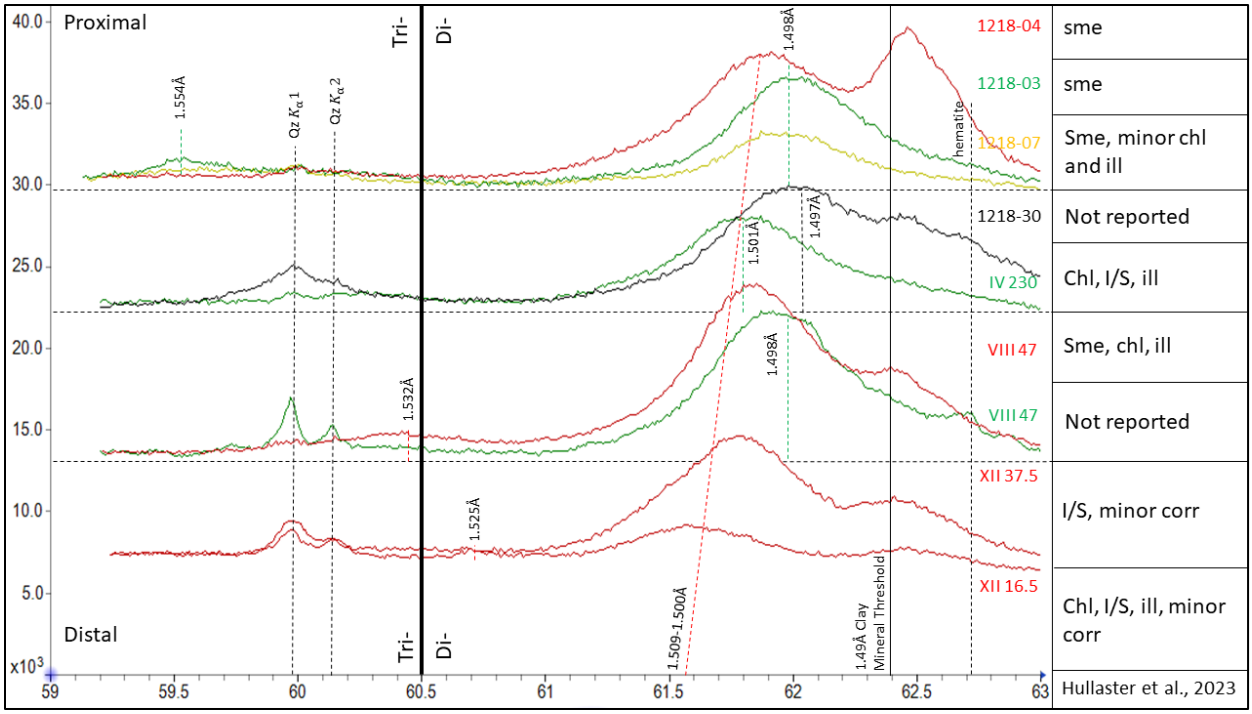

Figure 8 – Overlay of random clay fraction XRD spectra from the proximal-most samples to the Uncompahgre Front (top) to the southwest distal red beds (bottom). The thick solid line at 60.5º 2Θ separates the trioctahedral and dioctahedral domains of clay minerals with the second solid line marking the threshold described in Moore and Reynolds (1988) for clay mineral 060 reflections. Peaks of significance are labelled and marked with dashed lines corresponding to the color of the sample and noted in Table 2. The right column reports data presented in Hullaster et al. (2023) of oriented clay fraction XRD for use in interpreting the random mount XRD.

The random mount clay fraction XRD was conducted to elucidate the octahedral sheet chemistry of clay minerals from red, green, and bleached samples (Fig. 8) of the Hullaster et al. (2023) identified clays (Fig. 8, right-hand column). Overall, the samples appear to be more of a dioctahedral character, indicating higher concentrations of trivalent cations, such as Al^{3+} and Fe^{3+}. Peaks that do not correspond to clay minerals include the ~1.485Å hematite peak near 62.5° 2θ and ~1.541Å quartz peak near 59.7º 2θ (Fig. 8, Table 2), corroborated by confirming their existence in full 2θ scans of the clay fraction and thus not focused on here (data not shown). Any other peaks below 1.49Å are disregarded as non-clay minerals as this is the lowest d-spacing correlating to 060 clay reflections (Moore and Reynolds, 1988).

Considering the dioctahedral region (60.5-63° 2θ), all red samples demonstrate two distinct peaks, referred to as a doublet hereafter. The dioctahedral 1.500Å peak for the proximal-most sample shifts to 1.509Å in the distal-most sample (Fig. 8, Table 2) while a ~1.487Å is consistently present as the secondary peak in the doublet. In contrast, the three green samples do not contain a clear dioctahedral doublet signature. The proximal-most green sample exhibits a single large dioctahedral peak at 1.498Å with an asymmetric long tail towards the high-angle side. The proximal-most bleached sample shows a similar asymmetric ~1.498Å peak with lower intensity. In increasingly distal samples, the center of the large dioctahedral peak shifts from

1.502Å in a red sample (1218-04) with smectite, to 1.511Å in a red sample that contained chlorite, illite, I/S, and corrensite distally (Fig. 8, Table 2).

For all samples, the intensity of peaks in the trioctahedral portion is much lower than the dioctahedral portion, with most samples having either small broad/diffuse signal or small identifiable peaks. The most prominent features are a doublet of peaks seen clearly in samples at ~1.541Å correlating to the quartz $K\alpha_{1\&2}$ (Table 2, Fig. 8). One proximal green sample (1218-03) that was determined to contain only smectite, has an anomalous 1.554Å peak that aligns with Fe-chlorites (Srodon et al., 2001) but no trioctahedral smectites as predicted by the oriented XRD (Hullaster et al., 2023). We see little evidence for biotite within the <2 µm clay fraction, as it should give an 060 peak at ~1.538Å.

Table 2 – Random XRD diagnostic 060 clay peak values and corresponding clays identified by Hullaster et al. (2023). Additional non-clay peaks correspond to quartz (1.54…) and hematite (1.48…). Clays from Morrison and Parry incorporated and listed at the bottom of the table with "BI" notation.

	Major *060* clay XRD peak locations		**Major non-clay reflections**	**Hullaster et al. (2023)**
Sample	**Tri- d060 values (Å)**	**Di- d060 values (Å)**	**d-spacing (Å)**	**Identified clays**
1218-04 red	-	1.500	1.5415,1.487	Sme
1218-03 green	1.554	1.498	1.484	Sme
1218-07 bleach	-	1.512 (weak)/1.498	1.5415,1.484	Sme>Chl, Ilt
1218-30 black	1.534 (weak)	1.497	1.541, 1.487	Not reported
IV-230 green	-	1.501	1.5415, 1.483	Chl, I/S, Ilt
VIII-47 red	1.532(weak)	1.500	1.5415, 1.487	Sme>Chl, Ilt
VIII-47 green	-	1.498	1.5415, 1.483	Sme (not reported)
XII-16.5 red	1.525 (weak)	1.509(weak)/1.504	1.5415, 1.487	Chl, IS, Ilt, Corr
XII-37.5 red	-	1.501	1.541, 1.486	IS, Corr
	From Morrison and Parry (1986)			
BI-15	-	1.506/1.501		CS + IS
BI-1-13	-	1.506/1.502		CS + IS
BI-1-4	-	1.508/1.505		CS + IS
BI-6	-	1.507		CS

Corrensite, "normally" a trioctahedral coordinated clay mineral consisting of randomly interlayered chlorite and smectite layers, has been reported in XRD findings demonstrating a

doublet signal but of a dioctahedral nature (Table 2; Morrison and Parry, 1986). The samples with reported corrensite occur in the distal section XII samples here and the random XRD reveals no doublets within these samples that correlate to a dioctahedral smectite and chlorite peak but rather non-clay minerals and dioctahedral smectite (Fig. 8; Table 2).

Thermal and Temporal Signatures

Epidote Authigenesis

In addition to clays produced via biotite alteration, epidote is a common index mineral found as an accessory phase in proximal Cutler Formation samples. In hydrothermal systems, epidote forms in high temperature (>200ºC) intermediate to alkaline alteration conditions when coexisting with chlorite and Na-plagioclase (Inoue, 1995) and often exhibits variable Al^{+3} for Fe^{+3} substitution during growth that leads to distinct zoning (Bird and Speiler, 2004). The surface textures of ~100 epidote grains from this proximal 1218-03 green and ~100 from distal XII 37.5 red were analyzed to elucidate evidence of authigenesis chemically and texturally as growth domains on the grain boundary or interior. No clear evidence for overgrowths, Al/Fe zoning, or evidence of euhedral crystals that formed in-place was observed. The boundaries of both green and red epidote grains demonstrate similar aluminum enrichment behavior, seen distinctly in the elemental map (Fig. 9, left) but not the line scan across the grain interior (Fig. 9, right). Considering the aluminum enrichment also observed in the secondary products of biotite alteration (Fig. 6 and 7) and the similar enrichment of Si in the elemental map of the grain (Fig. 9, left) indicates this may be a significant finding; however, the use of 0.3 µm alumina polishing powder during preparation of the grain mounts may be the source of zonation observed here, especially considering the aluminum zoning is seen in epidotes from both green and red rock samples.

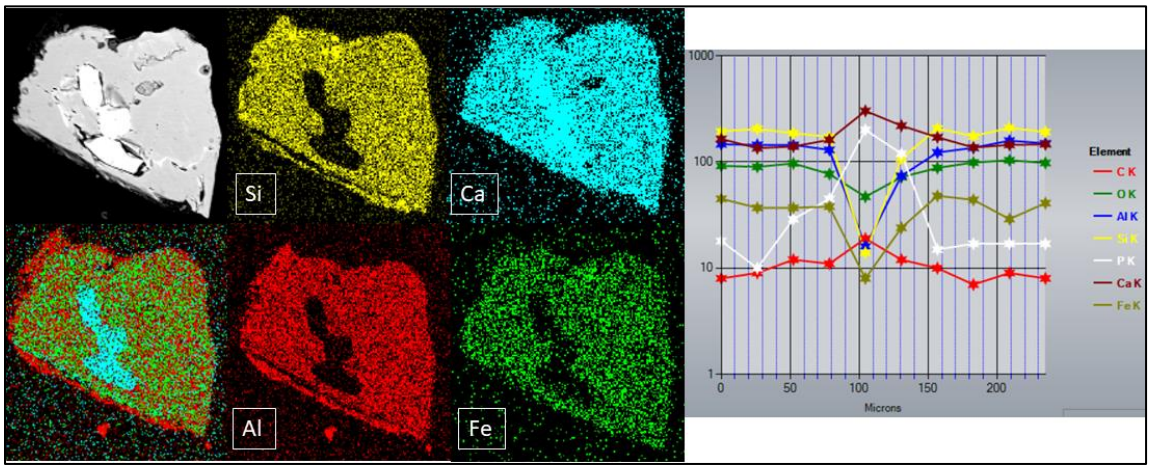

Figure 9 – XII 37.5 red sample SEM-EDS elemental maps (left) and linescan (right) of epidote grain with apatite inclusion and aluminous rims. The greyscale (top left) shows the grain texture for comparison with the following elemental maps. The lower left square represents a composite of all elements overlain on the greyscale image.

Fig. 10 shows an anomalous texture in which biotite appears to exist in equilibrium with epidote. The backscattered electron image (Fig. 10, left) shows the biotite layers parallel to a fracture in the surrounding epidote grain. Additionally, a smaller epidote crystal (near point 4 in the image) is intergrown between the biotite layers. The chemistry of the larger and smaller epidotes appears

nearly identical via EDS (Fig 10, right, points 1 and 4, respectively). The main chemical differences of significance to both mineral structures are magnesium and potassium, solely in biotite (spectra 2 and 3), and calcium, in the epidote. Our SEM results of altered biotites (Fig. 6) demonstrated that the main alteration process occurring in biotite interlayers is potassium replacement with calcium, which is not taking place in the grain from the green sample here (Fig. 10). The iron is not incorporated into either mineral preferentially. No distinct trends can be seen in the chemistry of epidote adjacent to the biotite. Also seen among the epidote grains are a multitude of minerals as intergrowths consisting of apatite, quartz, and titanite as well as biotite (Fig. 9 and 10). The paragenetic association among the epidote and inclusion minerals mentioned was not a focus of this study.

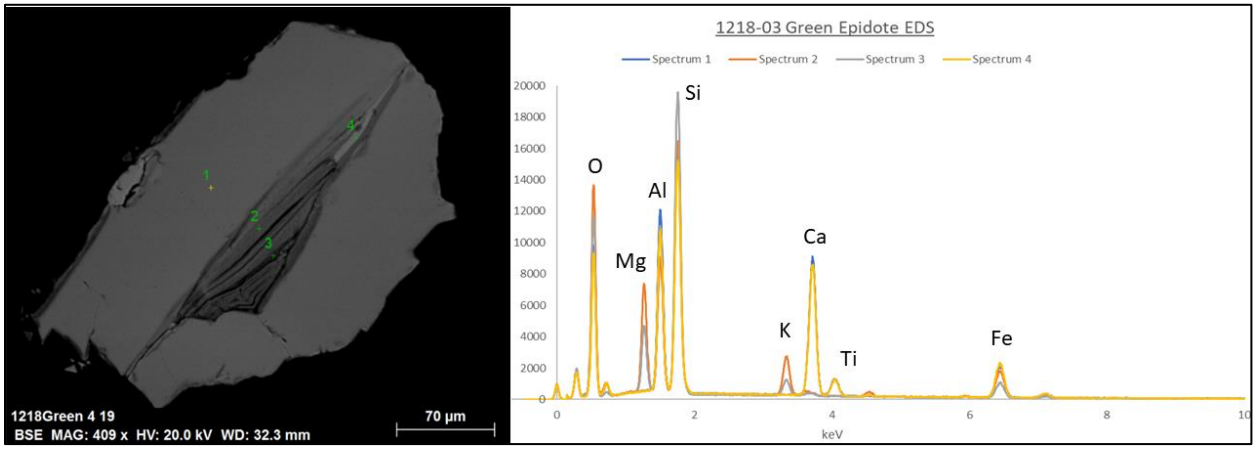

Figure 10 – 1218-03 green sample SEM photomicrograph of epidote surrounding biotite grain with corresponding points for EDS collection (left). Overlay of spectra from SEM-EDS points in photomicrograph with the associated element for each peak (right)

Apatite Fission-Track Analysis

The two samples, proximal green (1218-03) and distal red (63S-XII-37.5) yielded Oligocene AFT ages of 25.5 ± 2.5 Ma and 27.2 ± 2.7 Ma, respectively (Figure 9; Table 3). Confined fission tracks were measured from both samples and yielded mean track lengths (MTL) of 10.38 ± 0.2 μm (1218-03 green) and 10.67 ± 2.6 μm (63S-XII-37.5 red).

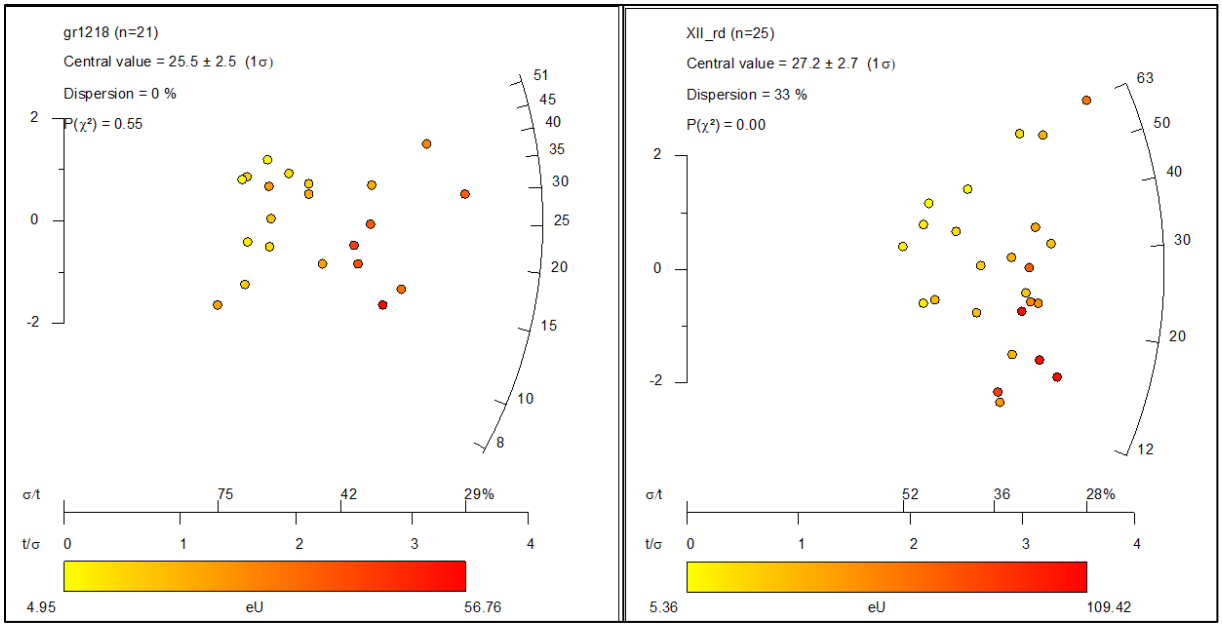

Figure 11 – Radial Plot and MTL measurements. Radial plot provides a central age based on single-grain ages and associated uncertainty. MTL histograms show the expected (red) and predicted (grey) curves for the model fit to the MTL distribution as a validity check.

Table 3 - Summary of laser ablation apatite fission track data. n=number of grains dated, Ns=number of spontaneous tracks counted, ρs=average spontaneous track density ($x10^5 cm^{-2}$), 238U=average uranium concentration of the analyzed grains, $P(\chi^2)$= χ^2 probability after (Vermeesch, 2009), t=central age (Ma), Dpar=mean track etch pit diameter parallel to the crystallographic c-axis, P=pooled age, #=number of confined tracks counted, MTL=mean of measured confined tracks in microns and ±1σ is also in microns.

Sample	n	Ns	ρs	238U (ppm)	P (χ^2)	t ± 1σ (Ma)	Dpar (μm)	P ± 1σ (Ma)	#	MTL ± 1σ (μm)
1218-03 Green	21	181	2.1	17.4	0.55	25.5 ± 2.5	2	23.2 ± 6.3	90	10.38 ± 0.2
63S XII 37.5 Red	25	416	4.1	36.5	0	27.2 ± 2.7	2	24.7 ± 6.0	90	10.67 ± 2.6

Zircon (U-Th)/He Analysis

Two samples were selected for ZHe analysis, samples 1218-03 green (4 grains) and 63S-XII-37.5 red (5 grains) exhibited a large spread in single-grain ages (Table 4). Sample 1218-03 displayed a range of ages from 141.04 ± 2.43 Ma to 577.1 ± 7.9 Ma and sample 63S-XII-37.5 yielded ages from 94.57 ± 1.32 Ma to 624.73 ± 8.46 Ma (Table 4). All ages are older than deposition except for 2 grains within the red sample, with an age population of 102.2 ± 7.6 Ma, and 1 grain in the green sample with a slightly older age of 141.0 ± 2.4 Ma.

Table 4 – Single grain zircon-He ages. eU: effective uranium scaled for relative alpha production rate, FT: fraction total, Corr Age: corrected age with 1 standard deviation of error, and mass and elemental concentrations of the analyzed grain are provided.

Sample	#	U (ppm)	Th (ppm)	eU (ppm)	FT	He (ncc)	Mass x10^6g	Raw Age ± 1σ (Ma)	Corr Age ± 1σ (Ma)
1218-03 Green	1	388.1	241.3	444.8	0.80	701.4	4.93	285.3 ± 3.6	358.7 ± 4.6
	2	151.2	77.0	169.3	0.75	414.4	2.72	436.8 ± 5.9	577.1 ± 7.9
	3	650.6	515.9	771.8	0.79	462.6	2.92	110.1 ± 1.9	141.0 ± 2.4
	4	253.9	174.3	294.8	0.71	457.3	1.76	280.2 ± 3.7	395.9 ± 5.4
63S XII 37.5 Red	1	577.5	262.0	639.1	0.73	271.8	1.44	78.4 ± 1.0	107.2 ± 1.4
	2	327.2	127.7	357.2	0.69	125.2	1.78	64.7 ± 0.9	94.6 ± 1.3
	3	220.9	100.6	244.5	0.71	601.7	2.28	438.9 ± 5.8	611.8 ± 8.3
	4	263.4	85.2	283.4	0.78	572.0	3.67	362.4 ± 4.9	464.2 ± 6.3
	5	205.1	93.6	227.1	0.77	618.1	4.95	483.6 ± 6.4	624.7 ± 8.5

Thermal History Modeling

Thermal history modeling was performed on samples 1218-03 Green and 63S XII 37.5 Red (Figure 12 and 13). These samples comprise the end points of a lateral transect within Permian Cutler clastics extending from the mouth of Unaweep Canyon at the Uncompahgre Front to the distal red beds ~10 km southwest (Fig. 2 and 4). Confined track distributions, individual models, modeling parameters, and ZHe data are available in Figures 11-13 and Tables 3 and 4. ZHe data was modelled with AFT to understand the timing and temperature of maximum burial of Cutler sediments. The more recent Cenozoic history was modelled using only the AFT age and confined track data to better resolve the lower temperature cooling history.

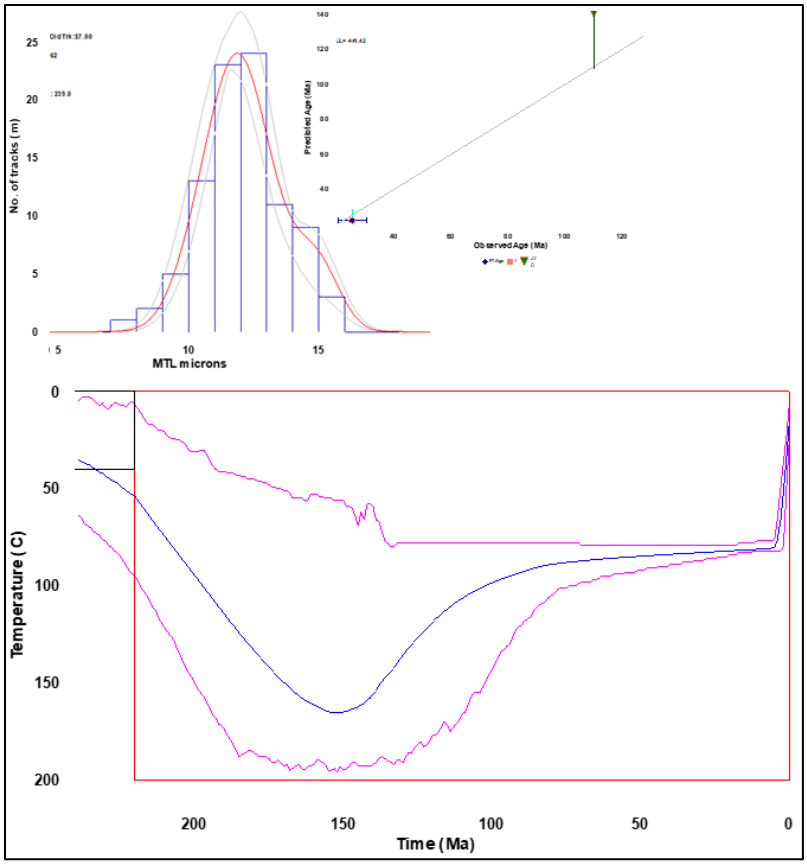

Figure 12 – QTQt model of proximal 1218-03 green demonstrating maximum burial occurring ~150 Ma and to temperatures of ~180 ºC. MTL histogram and the observed-predicted summary for the model are also included and suggest poor fit against both the apatite fission-track and zircon (U-Th)/He data

The thermal history models yielded consistent time-temperature pathways for both samples, with two Cenozoic periods of cooling separated by a heating event: (1) cooling following maximum burial/temperature of ~180 ºC at ~150 Ma (2) reheating event which began at ~27 Ma and (3) Pliocene cooling to upper-crustal temperatures. The green sample began cooling at 45 Ma from ~120 ± 20 °C to ~40 °C at 25 Ma. In comparison, the distal red sample experienced a slight lag in the onset of the first cooling event, from ~115 ± 20 °C at 40 Ma to ~70 °C at 27 Ma. (Figure 10). Cooling rates for this first event are 4 °C/Myr and 3.5 °C/Myr for the green and red samples, respectively. After this phase of rapid cooling, both samples experienced minor reheating. The degree of reheating in the green sample is from ~40°C at 25 Ma to 80°C at 4 Ma giving a rate of 1.9°C/Myr. The red sample heated from ~70°C at 27 Ma to 80°C at 5 Ma for a rate of 0.45°C/Myr. Finally, both samples show a Pliocene cooling event took both samples from ~80°C at 5 Ma to surface conditions of 20 ± 20°C at a rate of 12°C/Myr.

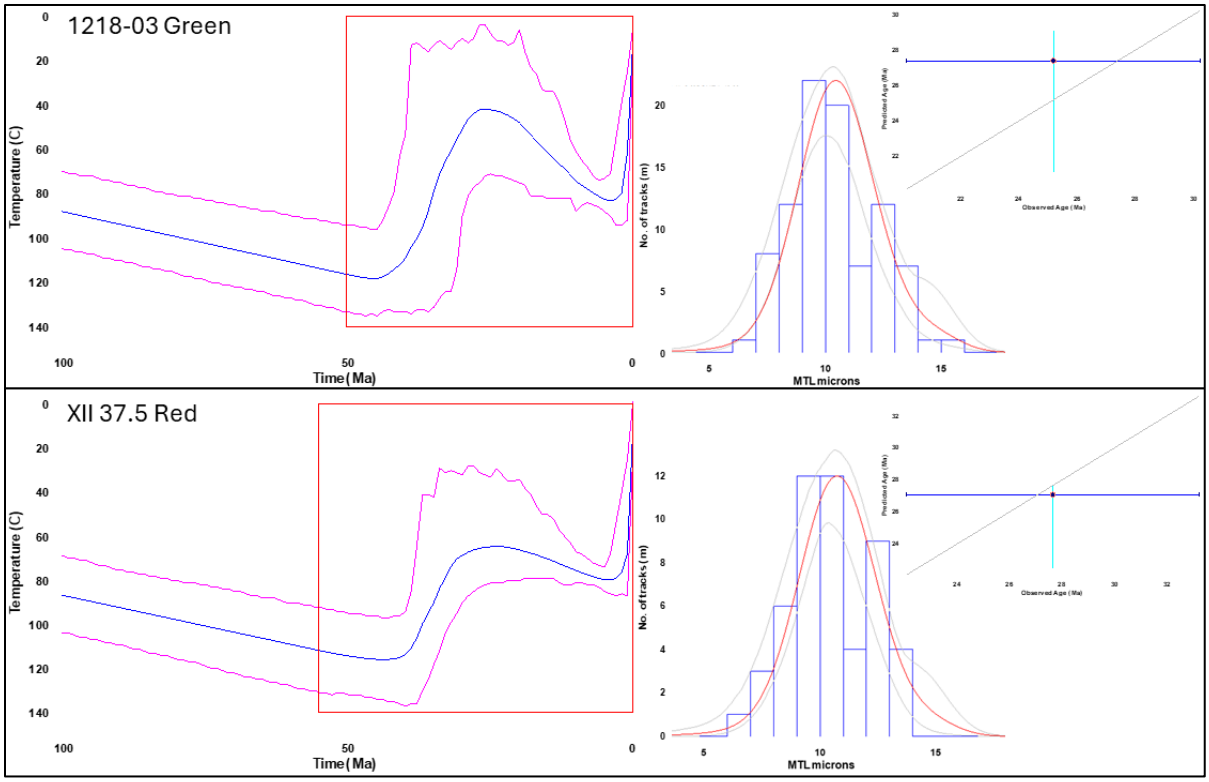

Figure 13 – QTQt time-temperature inversion models of proximal 1218-03 green and distal XII 37.5 red samples. MTL histograms show measured distribution of confined lengths and the associated model fit (red and grey curves). Observed vs. predicted age for the apatite fission-track data showing a close agreement of cooling pathway to input data.

Discussion

Here I integrate clay mineralogical and low-temperature thermochronology to help elucidate paleofluid alteration and the evolution of these signatures in the proximal Cutler Formation and how it fits into the larger scale evolution of the Colorado and Uncompahgre plateaus. Dutta and Suttner (1986) and Suttner and Dutta (1986) employed combined bulk and clay mineralogy of proximal Cutler Formation samples to propose diagenetic and (Permian) paleoclimatic signatures without attribution to thermal events. However, my work and that of Hullaster et al. (2023) provide evidence that the signatures recorded in clay minerals were greatly influenced by burial and post-burial magmatic or basinal fluids that overprint and thus complicate or even obliterate any paleoclimatic signal. Complimentary datasets of regional temperature exposure with their likely alteration fluids with the clay/mineral chemistry evident in red, red/green, and red/bleached rock layers allow for a better understanding of the proximal Cutler Formation history.

Mineral Texture and Chemistry

Field- and laboratory-based observations suggest distinct differences in the post depositional histories of the red, green, and bleached samples. Color differences at the outcrop scale correlate with distinct trends in mineral texture and chemistry at microscopic scales. The question remains whether the alteration paths, evidenced by octahedral and interlayer chemistry trends, represent different processes or the same process progressed to various degrees among the samples with

different colors. Hullaster et al. (2023) proposed that similar reducing fluid events impacted both green- and bleached samples differently due to variations in grain size; additionally, there are no examples in the field where bleached and green layers are gradational or co-located, which argues that these colors record different geologic processes, with the red-green layers occurring lower in the section and more proximally than the red-bleached layers.

Petrographic observations confirm that alteration observed in the green and bleached samples varies from that in the red samples in terms of both texture and alteration products (Fig. 5). Similar macroscopic textures occur in all samples, such as the frayed grain edges and associated authigenic mineralization/ transformation. The alteration products of this texture vary from low birefringent clays with no distinct optical properties (red grains; Fig. 5E, F) to clear chloritization propagating into biotite grains (green and bleached grains; Fig. 5A, B, G, H) similar to the chloritization described by Parneix et al. (1985) in hydrothermally altered granites which were replaced by corrensite and chlorite. My study does not document any growth on 001 biotite planes. Macroscopic texture variations can be seen in greater chloritization propagating from the edge along the 00l plane of biotite and/or whole grain neoformation into chloritic minerals (Fig. 5G, H) compared to retention of the biotite optical properties in combination with transformed chlorite layers (Fig. 5A, B). Depending on the conditions, secondary mineralization related to biotite alteration consists of titanite and magnetite in diagenetic rocks and calcite, rutile, or anatase in higher-grade metamorphosed rocks (Jiang and Peacor, 1994) with secondary intergrowths in the Cutler Formation biotites consisting of Fe and Fe-Ti oxides observed petrographically and apatite seen in SEM-EDS of a bleached biotite more indicative of a burial diagenetic history.

Biotite alteration is associated with Mg depletion in green samples, Fe depletion in bleached samples, and Al enrichment in all samples compared to the original biotite chemistry (Fig. 8). Stable iron concentrations in green samples rather than an increase from original biotite chemistry may indicate in-situ transformation of ferric iron to ferrous iron, whereas reduced ferric iron in bleached samples was flushed from the immediate grain area. This interpretation is supported by Mössbauer spectroscopy performed by Hullaster et al. (2023), who showed Fe(II) and Fe(III) in the clay fraction in green but predominately Fe(III) in bleached rock samples. In some cases, the layers surrounding the bleached layers in the field seem to be enriched in Fe-oxides, indicating nearby reoxidation, whereas some mobile iron may have exited the proximal Cutler system altogether.

The random-mount XRD provides additional information regarding the chemical composition of the clays and the oxidation state of iron. Trivalent ions such as Al^{+3} and Fe^{+3} form dominantly 'dioctahedral' sheets that have generally smaller *d*-spacings than 'trioctahedral' clays containing dominantly divalent Mg^{+2} and Fe^{+2}. Given the color and corroborating spectral evidence for Fe(II) in the green samples, along with relatively common occurrences of chlorite and chlorite-smectite mixed layers that are commonly trioctahedral, we anticipated a significant distribution of trioctahedral clays. The XRD results here indicate a dominantly dioctahedral nature of the clay minerals with nearly all peaks in the trioctahedral 2θ range belonging to quartz. One single proximal green grain does demonstrate a potential Fe-chlorite peak at 1.554Å; however, the oriented XRD demonstrates an abundance of smectite in this sample. The red sample peak shifts in the dioctahedral portion from 1.500Å to 1.509Å in distal samples (Fig. 6, Table 2) likely

indicate that the larger Fe^{3+} is being incorporated into the mostly red samples distally compared to more aluminous incorporation proximally indicating that this alteration may be concentrated near the Uncompahgre Front. No doublet of clay minerals occur in the XRD here, similar to Morrison and Parry (1986), for describing the occurrence of corrensite in the samples; however, broad peaks with asymmetrical tails in a similar 2θ range and similar d-spacings may demonstrate a similar di-/di- coordination of the chlorite and smectite layers within corrensite. The heavy alteration sustained by the samples and the larger grain size of detrital biotite explains the lack of peaks in the random XRD.

The chemical changes observed in the secondary products of biotite alteration corroborate this finding. Although no increase in Fe occurs within the green alteration products, the concentration is much higher in green samples relative to bleached samples. The loss of Mg and retention of Fe observed in the octahedral composition of the green samples moves its composition in the direction of the CMS corrensite (CorWa-1), although with additional Al enrichment. Previously, the presence of regularly-interstratified mixed-layer chlorite (such as corrensite) was noted by Hullaster et al. (2023) in scattered red-, green-, and bleached proximal Cutler samples but Hullaster et al. (2023) were unable to classify the nature of the clay structure. Morrison and Parry (1986), near the Lisbon Fault (UT), described a di-/di- nature to their identified corrensite due to doublet peaks at ~1.508/1.501 (Table 2) and proposed an acidic fluid alteration path due to the presence of kaolinite. We do not observe kaolinite here likely due to the difference in source rocks – that is, the presence of biotite-rich basement in our proximal study region compared to more mineralogically mature lithologies of Cutler Formation in their study region. We do observe I/S, illite, smectite, and chlorite found within the "clayey zone" described by Inoue (1995). This assemblage can be indicative of some acidic influence in the system wherein aluminum was mobilized. Additional evidence is contained in quartz cement and transformed layers within biotite, indicating quartz could have been a pressure-solution phase during this type of alteration in the Cutler system.

The bleached samples appear more similar to the Cutler Formation bleached samples analyzed by Morrison and Parry (1986) near the Lisbon Valley fault (UT) and the La Sal Laccolith (Fig. 2 and 7). These authors described a dioctahedral Al-rich corrensite influenced by hydrothermal activity, contrary to the depositional trioctahedral corrensite described by Dutta and Suttner (1986) and similar to the green samples we report here. This dioctahedral signature indicates an intermediate to weakly acidic pH alteration condition at temperatures <200ºC based also on association with the observed chlorite, C/S, and the general smectite dominance.

Epidote should be concentrated, by authigenesis, at temperatures >200ºC (Inoue, 1995). Hullaster et al., (2023; Fig. 7) found epidote concentrated in green relative to red- and bleached samples, with textural evidence of growth from a clay mineral. The mounts analyzed in this present study were done after removing epidote from the rock and thus we do not preserve the original rock fabric and the association with adjacent minerals. The analyzed grains did not demonstrate authigenic growth relic of high temperature alteration, similar to Bird and Spieler (2004), and more resembles deformation due to compaction over authigenic growth (Fig. 16). The maximum temperature achieved (~180 ºC) during maximum burial would be the only event capable of producing the temperatures required to meet an intermediate alteration series and associated mineral assemblage. The middle Cenozoic heating event impacted both proximal and distal samples in this present study but did not achieve as high of temperatures – max ~80 ºC

(Fig. 12 and 13). The more likely mineral assemblage seen in the Cutler Formation samples indicate a chlorite, smectite, and their mixed layer counterparts within an intermediate alteration series. Na additions occur almost solely in the bleached samples and evince a separate event of more sodic concentrations within an alkaline alteration series. Inoue (1995) also noted that the Na series within an alkaline alteration path may occur with a Ca-Mg alteration series and seen almost entirely in bleached grain interlayer structure (Fig. 7, right).

Corrensite is formed geologically in saline, terrestrial, and marine deposits and a common alteration product of biotite and can occur in a wide range of temperatures (as low as 60ºC) and rock types (Chang et al., 1986 and Reynolds, 1988). Sugimoto et al. (2008) found that when biotite alteration proceeded under anoxic conditions Fe(II)-rich corrensite (trioctahedral) was formed. Dioctahedral corrensite, with higher Al:Mg ratio, and doublet XRD peaks in the dioctahedral portion of XRD, from Lisbon Valley (UT) bleached sandstones was determined to have a smectite precursor (Morrison and Parry, 1986). Our study demonstrates a similar dioctahedral coordination in the XRD but with an absence in doublets. SEM-EDS of biotite alteration confirmed Fe conservation in green samples and Al enrichment in all samples. Tosudite is much more restricted to hydrothermal type alteration of intermediate to acidic igneous rocks, compared to the more unrestricted formation conditions of corrensite (Reynolds, 1988). XRD spectra for corrensite and tosudite are extremely similar differing mostly in intensity (Reynolds, 1988) and in the case of Cutler sediments and results presented in Hullaster et al. (2023)(Fig. 14) the I(006) is greater than I(004) indicating more likely a low-Fe dioctahedral species.

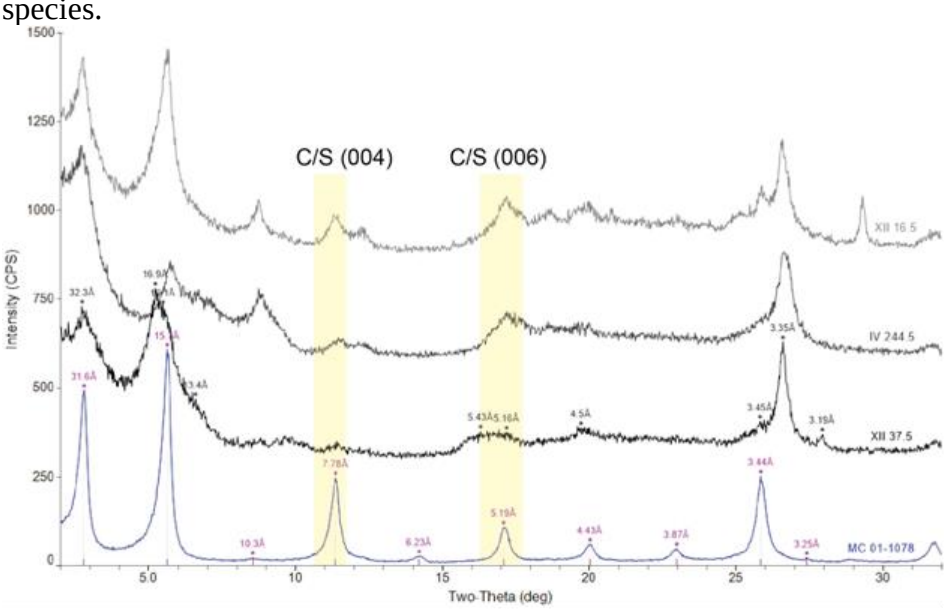

Figure 14 – (From Hullaster et al., 2023) XRD overlay for samples containing corrensite superstructure peaks. The 004/006 reflection intensity relationship is highlight for comparison.

Looking at the chemistry of the bleached clays analyzed by Morrison and Parry (1986) and the CMS standard clay chemistry near the Lisbon Valley fault (UT) with respect to our bleached clays they do overlap in octahedral chemistry. I suggest that the bleaching events experienced by our study region (Al enrichment and Fe depletion) correlate with La Sal bleaching described by Morrison and Parry (1986) with the green trend seen in this study belonging to a separate event affiliated with reduced fluid, likely sulfate-rich basinal brines (Hullaster et al., 2023). The input

of Na shows up in the chemistry of all of the bleached alteration samples (Fig. 7 right), with one green sample showing strong sodium input. The Ca and Na could be coming from plagioclase dissolution or reactive fluids/brines. Deep basinal brines are typically rich in Na, including those associated with dissolution of salts of the Honaker Trail Formation which lies beneath the Cutler Formation. Deep Paradox Basin brines have high concentrations of Na, Ca, Mg, and K, with Na generally much higher, but originate via a variety of processes that lead to regional variations (Kim et al., 2022). Generally, the brines are depleted in Mg and K due to water-rock interactions during burial diagenesis (Kim et al., 2022). Elsewhere in the Paradox Basin, Kim et al., (2022) observed hairy illite precipitation associated with bleaching of redbed Navajo Sandstone; however, our samples demonstrate a lack of illite and a chemical trend of potassium depletion among the biotite alteration products.

In general, the assemblage of clay minerals in the proximal Cutler Formation and their interlayer chemistry indicates the influence of intermediate Ca-Mg type hydrothermal alteration rather than acidic or alkaline fluids (Inoue, 1995). The expected mineral assemblage and their respective formation temperatures for this series are depicted in Fig 15 (right). Further investigation into the nature of the aluminum enrichment observed in altered biotites is needed to explain its presence in an intermediate type alteration rather than acidic. Geyer (2024) found that aluminum was mobilized from clay minerals in the presence of near saturated brines up to temperatures of 100°C regardless of brine composition and acidity. Solubility of the aluminum could decrease and precipitate out as new aluminous minerals if the brines mixed with meteoric sources and became less saline.

Thermal and Temporal Signatures

Central to our understanding of paleoclimate and post-depositional processes in the Culter Formation is the maximum temperature experienced during burial and post-burial alteration. To constrain the maximum temperature, I performed low-temperature thermochronology on a distal red sample (63S XII 37.5) and a proximal green sample (1218-03). The Cutler Formation accumulated in the middle Pennsylvanian to early Permian and sourced from igneous and metamorphic suites of Precambrian basement of the Uncompahgre Plateau (Werner, 1974; Cater, 1970; Moore et al., 2008). There is little literature providing undisputed ages when deposition was occurring; tenuous ages ranging from ~310 – 290 Ma have been reported (Soreghan et al., 2014) and should be noted that implications of an absolute age date was not the focus of this study but rather providing context for the ages returned from thermochronological analyses. The proximal Cutler Formation is at the surface, and extends at depth, but has been proposed to have been buried by ~3 km of Mesozoic strata (Cater, 1955; White and Jacobson, 1983; Dutta and Suttner, 1986; Suttner and Dutta, 1986; Rønnevik et al., 2017).

Single-grain ZHe ages were highly dispersed and recorded ages both younger and older than the depositional age of the Cutler Formation for both the green/proximal and red/distal samples (Table 3). The grains younger than the age of deposition of the Cutler Formation are of Cretaceous age (100 Ma), suggesting that these rocks were within the zircon partial retention zone by at least the Cretaceous. These Mesozoic cooling ages are older than ZHe dating performed on samples of basement from the Uncompahgre Plateau which showed maximum burial in the latest Cretaceous (65-63 Ma; Rønnevik et al., 2017). The mixture of pre- and post-depositional cooling ages preserved in the Cutler Formation suggests that these samples likely

resided in or just below the zircon partial retention zone (~180ºC) for a prolonged period, ~10-15 myr. (Flowers et al., 2020). Thus, I suggest that these samples should have been buried to depths of ~6 km, assuming an elevated 25 – 30°C geothermal gradient of the Colorado Plateau and the burial temperatures provided by ZHe analyses.

The proximal green sample yielded an AFT central age of ~25 Ma and ~27 Ma in the distal red sample. Both samples are reset as their cooling age is younger than their associated depositional age. However, the green sample passed the chi squared test and showed lower dispersion. Whereas the red sample yielded high dispersion and a failed chi squared test, which indicates sources of uncertainty that are not accounted for in this central age population (Galbraith, 2005). The lower dispersion and passed chi squared suggests that the temperature experienced in the green grains was higher than that of the red to anneal the older grains and remove the dispersion (Galbraith, 2005). Rønnevik et al. (2017) yielded Oligocene AFT ages from Unaweep Canyon basement rocks and the NE margin of the Uncompahgre Plateau, consistent with the cooling ages identified in this study. The emplacement of the Oligocene (~30 Ma) La Sal Laccolith has been suggested as a control on the thermal evolution of the Uncompahgre region (Rønnevik et al., 2017). Bailey et al. (2021) studied the adjacent Paradox Basin, however, and found Eocene exhumation was occurring prior to La Sal emplacement. The regional AFT (Rønnevik et al., 2017, and this present study) correlates with zircon U-Pb crystallization ages of the La Sal laccolith emplacement indicating this geologic event propagated heat into the proximal Cutler Formation and Uncompahgre Plateau.

To estimate paleotemperature evolution of the Cutler Formation I conducted thermal history modelling on a distal red- and proximal green-sample (Fig. 12). Thermal history modelling reveals that both the red and green samples underwent similar Mesozoic – Cenozoic heating and cooling in the Eocene – Oligocene and Pliocene. Following Pennsylvanian – Permian deposition, the Cutler Formation was heated to ~180 ºC by Jurassic time indicating no more than 6 km burial depths, considering a geothermal gradient of 25 – 30 ºC/km, for an extended period of time to only partially reset the ZHe ages. This value is much greater than previous estimations of burial on the Cutler Formation of ~2.4-3 km (Suttner and Dutta, 1986). The Mesozoic strata is mostly missing in the proximal Cutler Formation region but according to sedimentary units such as the Book Cliffs in the Colorado Plateau and AFT track modelling of the Mesozoic strata on the Uncompahgre Plateau indicates ~3 km of missing strata (Gualtieri, 1988; Rønnevik et al., 2017). These thicknesses are consistent with the ZHe and burial data in this present study.

Following peak burial temperatures, the Cutler Formation experienced a period of rapid cooling in the Eocene – Oligocene. This period of cooling is younger than timing of initial exhumation from the Uncompahgre (~70 – 60 Ma), White River (~50 Ma), and Monument (~50 Ma) uplifts (Naeser et al., 2002; Rønnevik et al., 2017; Murray et al., 2019). The Paleocene – Eocene deposits (Wasatch and Green River Formations), estimated according to geologic mapping is ~1km (Gualtieri, 1988; Rønnevik et al., 2017). Given the location of the Cutler samples, in a downthrown block of the Uncompahgre reverse fault, the younger exhumation suggests delayed denudation due to regional, fault-associated uplift.

There is a heating delay from emplacement of the Laccoliths (~29 Ma) and onset of the middle Cenozoic heating event in the proximal Cutler Formation (~25 Ma) making their correlation

ambiguous. The result of this heating event can be seen to a higher degree in the proximal green sample relative to the red sample of which I suggest indicates heated fluids had to travel through subsurface fault networks before interacting with more proximal samples and/or the geothermal gradient of the Plateau increased during the regional magmatic flare-up. Murray et al. (2019) found that in sedimentary samples collected from Jurassic sandstones ~10 km away from Henry Mountain laccolithic activity in southeastern Utah and Colorado Plateau, AFT ages were not reset following middle Cenozoic heating, but the Permian rocks ~1 km deeper did experience age resetting at this time. The Permian rocks studied here, over 30 km from the La Sal Laccolith experienced extensive interaction with this middle Cenozoic heating event, either through heated fluid interactions or a regional increase in geothermal gradient which would have remained until the second stage regional exhumation attributed to the incorporation of the Colorado River headwaters and evidenced by increased incision rates of uplifted areas in the Pliocene (Rønnevik et al., 2017, Murray et al., 2019, Bailey et al., 2021).

Synthesis and Conclusion:

Clay- and heavy (apatite, zircon, epidote) minerals within sedimentary deposits of the Proximal Cutler Formation near the Uncompahgre Plateau (paleo uplift) hold the chemical signatures of the history of diagenetic- and thermal events here. These signatures are complex and require the synthesis of several datasets due to variations in clay chemistry. Correlation of the burial, reheating, and exhumation conditions with the biotite alteration textures and secondary products enables formation conditions to be estimated according to the rock colors and potentially distinct geologic events.

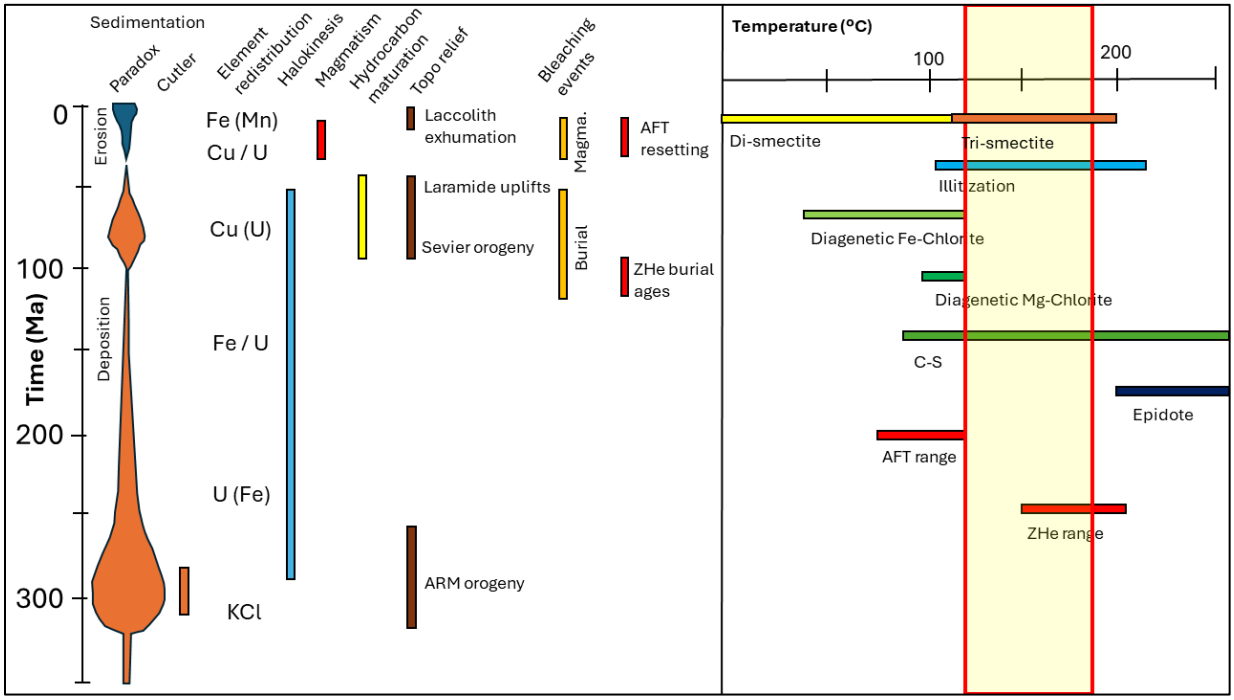

Figure 15– Comparison of timing of events within the Paradox basin and its relation to proximal Cutler sediments (left: modified from Barton et al., 2018). Timing and magnitude of sedimentation/erosion of the Paradox Basin seen by the orange/blue polygons, respectively, and the adjacent orange rectangle represents Cutler Fm. deposition according to Soreghan et al.

(2014). Timing and type of element being redistributed is shown. Vertical polygons for halokinesis, regional magmatism, hydrocarbon maturation, bleaching, and relief forming/orogenic events demonstrate the timing of each event. Timing of values returned from AFT and ZHe results from our samples are included (left). Right: Temperature ranges of mineralogic comparisons made in this study, the closure temperature ranges of AFT and ZHe. The yellow box highlights the range of maximum temperatures experienced by the red, green, and bleached sediments during burial and post-burial alteration.

Considering the thermal history models, partial resetting of single grain ZHe ages, and a lack of epidote authigenesis suggest that maximum temperatures of ~180 ºC occurred during maximum burial at ~150 Ma. Assuming a geothermal gradient of 25 – 30 ºC, an estimated ~6 km of burial is suggested for the proximal Cutler Formation. The temperatures and depth measured for samples in this study is significant enough to expect all dioctahedral smectite to be converted to illite-smecite then illite – a transition that is typically complete by ~4 – 5 km depth (Meunier, 2005) if an adequate supply of potassium is provided, perhaps through K-feldspar dissolution. These burial estimates far exceed previous estimates from the region and indicate that any climate signatures housed in the clay minerals have likely been reset. Furthermore, the burial temperatures reported here suggest the frequent occurrence of mixed layer illite-smectite and chlorite-smectite throughout the study area in red, green, and bleached samples likely formed during burial diagenesis (Fig. 15). On the other hand, the high concentration of dioctahedral smectite and chlorite, and random and ordered mixed layer C/S in proximal Cutler sediments both proximal and distal to the Uncompahgre front. This indicates the strong presence of fluid interaction post maximum burial (Fig. 15) due to burial not accounting for the mineral assemblage. Chlorite-smectite mixed layer minerals form through hydrothermal activity from temperatures as low as 80 ºC and >200 ºC (Fig. 15, Reynolds, 1988; Jiang and Peacor, 1994), suggesting the presence of regular ordered C/S could be explained by heating during burial.

Modern proximal Cutler Formation rocks are smectite-rich and consistent with temperatures of either basinal or meteoric waters due to temperature sensitivity of smectite (Bettison-Varga et al., 1991; Meunier, 2005; Beaufort et al., 2015) and the timing of cooling into the smectite stability zone following maximum burial (Fig. 15). The increased temperature following Eocene – Oligocene uplift undergone by the proximal green sample relative to the distal red sample indicates the presence of heat-related fluids rather than increased geothermal gradient due to distinctions among the proximal and distal regions here. The closer proximity of the green sample to the Uncompaghre-bounding faults suggests that these hydrothermal fluids are being transmitted through fault conduits in the subsurface and interacting with proximal Cutler Formation sediments moreso than the distal samples.

This work added new constraints to understand the timing and mechanism of green and bleached color development in the proximal Cutler Formation in the context of the climate, sedimentary, and tectonic frameworks for this region. The color of the biotite alteration mirrors the overall color of the rock and relates to chemical variations among the differently colored samples. These data support the interpretation that the red/green and red/bleached layers were caused by fluid-rock interactions and facilitated by fault-associated transport of basinal fluids along the Uncompahgre front and subsequent interaction with the sedimentary rocks of the Cutler Formation. This work also demonstrates that the timing of the greening and bleaching followed

maximum burial in the Jurassic (Fig. 12), relating to tectonic, sedimentary, and climatic events in the Cenozoic.

Geochemical measurements from this study, while not conclusive, suggest that distinct processes contributed to forming the green and bleached layers through the action of reducing fluids. Evidence for the action of reducing fluids in the Cenozoic has been noted in other parts of the Paradox Basin, although none of the patterns of alteration mineralogy, chemistry, and texture clearly match those seen in the proximal Cutler Formation. Kim et al. (2022) noted that the recent laccolithic intrusions (30-20 Ma) and exhumation (post-5 Ma) of the Colorado Plateau could have contributed to the dynamic change in regional fluid flow dynamics and mixing of deeper circulating sulfide-rich brines with shallower deposits resulting in bleaching, while others showed evidence for hydrocarbon-derived bleaching (e.g., Bailey et al., 2022 and references therein). No organic material was observed here providing no evidence for petroleum associated fluids to have migrated through the proximal Cutler Formation or the signature was removed by later events. Furthermore, the proximal Cutler sediments do not show clear evidence for oxidation of sulfides left from reaction with sulfide-bearing brines, obscuring the nature of the reducing agent. In this study, the bleached altered biotite samples demonstrated both K → Na and K → Ca interlayer replacement, whereas most red and green samples only showed evidence for K→Ca replacement, outside of an outlier green grain pore which demonstrated K → Na then K → Ca. Whether or not this exhumation and fluid mixing imparting the Na signature caused the bleaching is unclear; however, it points to a signature of basinal brines flowing upward into the green and bleached layers along faults and lithologic contacts.

Future Work

Overall, the combination of the tectonic and sedimentological framework, source rock mineralogy, and climate drivers in the proximal Cutler Formation have resulted in overprinting signatures. Further unravelling of these signatures will provide insights into the various fluid-rock interactions that have created the geologically and economically critical locality within the Paradox Basin. To expand on the research demonstrated here, more work is needed with STEM-EDXA on oriented biotite samples to better understand biotite alteration and the dynamics of corrensite formation at the atomic scale. This will also provide better isolation of quantitative octahedral chemistry of the authigenic clays formed. Further insight into biotite alteration in the presence of brines will also provide insight into the chemical variations observed in this study Measurements of clay isotopes are needed to corroborate the existence of separate events leading to distinct authigenic clays among the different colored rocks; however, the lack of illite in Cutler samples may limit the sample population. Exploring the clay signatures on the other side of the Uncompahgre Plateau in both sedimentary and basement rocks may also provide evidence (for or against) for potential fluid pathways and chemistry influences from the Unaweep paleovalley or fluids propagating though subsurface faults and how that signature varies from our study. Additional thermochronology analyses need to be completed on bleached samples in order to understand red/green and red/bleached sample pair evolutions.

References:

Bailey L.R., Drake H., Whitehouse M.J., Reiners P.W. (2022) Characteristics and Consequences of Red Bed Bleaching by Hydrocarbon Migration: A Natural Example From the Entrada Sandstone, Southern Utah Geochem. Geophys Geosystems, 23. doi:10.1029/2022gc010465.

Bailey LR, Kirk J, Hemming SR, Krantz RW, and Reiners PW (2021). Eocene fault-controlled fluid flow and mineralization in the Paradox Basin, United States. Geology, 50(3) 326-330.

Banfield, J.F., & Eggleton, R.A. (1988). Transmission electron microscope study of biotite weathering. *Clays and Clay Minerals*, *36*(1), 47-60.

Barton, I. F., Barton, M. D., & Thorson, J. P. (2018) Paradox Basin fluids and Colorado Plateau copper, uranium, and vanadium deposits field trip. Society of Economic Geologists, 59. https://doi.org/10.5382/gb.59

Beaufort D., Rigault C., Billon S., Billault V., Inoue A., Inoue S. and Patrier P. (2015) Chlorite and chloritization processes through mixed-layer mineral series in low-temperature geological systems – a review. Clay Minerals, 50, 497–523.

Bettison-Varga, L., Mackinnon, I. D., & Schiffman, P. (1991) Integrated Tem, Xrd and Electron Microprobe investigation of mixed-layer chlorite-smectite from the point Sal Ophiolite, California. Journal of Metamorphic Geology, 9(6), 697–710. https://doi.org/10.1111/j.1525-1314.1991.tb00559.x

Bird D. K. and Spieler A. R. (2004) Epidote in Geothermal Systems. In *Epidotes* Reviews in Mineralogy and Geochemistry. Mineralogical Society of America. pp. 235–300.

Braun, J., van der Beek, P., & Batt, G. (2006) Quantitative thermochronology: Numerical methods for the interpretation of thermochronological data. Cambridge University Press. 10.1017/CBO9780511616433.

Case J.E. (1991) Geologic Map of the Northwestern Part of the Uncompahgre Uplift, Grand County, Utah, and Mesa County, Colorado, with Emphasis on Proterozoic rocks. U.S. Geological Survey, Miscellaneous Investigations, Series I-2088, 16 p.

Fagel, N. (2007) Clay Minerals, Deep Circulation, and Climate. Marine Geology, 130, 19–28.

Cater, F. W., & Craig, L.C.brind (1970) *Geology of the salt anticline region in southwestern Colorado*. United States Department of the Interior, Geological Survey.

Chang, H.K., Mackenzie, F.T. & Schoonmaker, J. (1986) Comparisons Between the Diagenesis of Dioctahedral and Trioctahedral Smectite, Brazilian Offshore Basins. Clays Clay Miner. 34, 407–423 https://doi.org/10.1346/CCMN.1986.0340408

Claeys P. F. and Mount J. F. (1991) Diagenetic origin of carbonate, sulfide and oxide inclusions in biotites of the Great Valley Group (Cretaceous), Sacramento Valley, California. Journal of Sedimentary Research **61**, 719–731.

Condon, S.M. (1997) Geology of the Pennsylvanian and Permian Cutler Group and Permian Kaibab Limestone in the Paradox Basin, Southeastern Utah and Southwestern Colorado. U.S. Geological Survey Bulletin 2000-P.

Copeland, P., Currie, C.A., Lawton, T.F., Murphy, M.A. (2017). Location, location, location: The variable lifespan of the Laramide orogeny. Geology. 45 (3): 223–226. doi: https://doi.org/10.1130/G38810.1

DeCelles, P. G. (2004). Late Jurassic to Eocene evolution of the Cordilleran thrust belt and foreland basin system, western U.S.A. American Journal of Science, 304(2), 105-168. https://doi.org/10.2475/ajs.304.2.105

Dickinson, W. and Snyder, W. (1978) Plate tectonics of the Laramide Orogeny. Geol. Soc. Am. Mem.. 151. 10.1130/MEM151-p355.

Donelick, R.A., OSullivan, P.B., & Ketcham, R.A. (2005) Apatite fission-track analysis. Reviews in Mineralogy and Geochemistry, 58(1), 49. https://doi.org/10.2138/rmg.2005.58.3

Dutta, P.K., Suttner, L.J. (1986) Alluvial sandstone composition and paleoclimate, II. Authigenic mineralogy. SEPM Journal of Sedimentary Research, Vol. 56. https://doi.org/10.1306/212f890e-2b24-11d7-8648000102c1865d

Erslev, E.A.. (1991) Trishear fault-propagation folding. *Geology*; 19 (6): 617–620. doi: https://doi.org/10.1130/0091-7613(1991)019<0617:TFPF>2.3.CO;2

Flowers, R.M., Macdonald, F.A., Siddoway, C.S., & Havranek, R.E. (2020) Diachronous development of Great Unconformities before Neoproterozoic Snowball Earth. Proceedings of the National Academy of Sciences, 117, 10172 - 10180.

Gallagher, K. (2012) Transdimensional inverse thermal history modeling for quantitative thermochronology. Journal of Geophysical Research: Solid Earth, 117(B2). https://doi.org/10.1029/2011JB008825

Gallagher, K., Brown, R., and Johnson, C. (1998) Fission Track Analysis and its Application to Geological Problems. Annual Review of Earth and Planetary Sciences. 26.519-572.10.1146/annurev.earth.26.1.519.

Geyer, C. (2024) Brine Driven Alteration of Phyllosilicates. Dissertation, University of Oklahoma, https://hdl.handle.net/11244/340271.

Gleadow, A. J. W., Harrison, M., Kohn, B. P., Lugo-Zazueta, R., & Phillips, D. (2015) The fish canyon tuff: A new look at an old low-temperature thermochronology standard. Earth and Planetary Science Letters, 424, 95–108. Retrieved from http://www.sciencedirect.com/science/article/pii/S0012821X15002927

Green, P.F., Duddy, I.R., Gleadow, A., Tingate, P.R., & Laslett, G.M. (1986) Thermal annealing of fission tracks in apatite: 1. A qualitative description. Chemical Geology: Isotope Geoscience Section, 59, 237-253.

Gualtieri, J., (1988), Geologic Map of the Westwater 30′ × 60′ Quadrangle, Grand and Uintah Counties, Utah and Garfield and Mesa Counties, Colorado: U.S. Geological Survey Miscellaneous Geologic Investigations Map I-1765, scale 1:100,000.

Guenthner, W.R., Reiners, P.W., Ketcham, R.A., Nasdala, L., & Giester, G. (2013). Helium diffusion in natural zircon: Radiation damage, anisotropy, and the interpretation of zircon (U-Th)/He thermochronology. *American Journal of Science*, *313*(3), 145-198.

Hasebe, N., Barbarand, J., Jarvis, K., Carter, A. & Hurford, A. J. (2004) Apatite fission-track chronometry using laser ablation ICP-MS, Chemical Geology, 207(3), 135– 145. http://www.sciencedirect.com/science/article/pii/S0009254104000427

Hoffman J. and Hower J. (1979) clay mineral assemblages as low grade metamorphic geothermometers: application to the thrust faulted disturbed belt of Montana, U.S.A. In *Aspects of Diagenesis* (eds. P. Scholle and P. Schluger). SEPM Special Publication. pp. 55–79.

Hullaster, D.P., Soreghan, G.S., Kukkadapu, R.K., Dumont, B.S., Dee, K.T., Elwood Madden, A.S.: Red-green-bleached redox interfaces in the proximal Permian Cutler redbeds: implications for regional fluid alteration (2023) Frontiers in Earth Science, 11, 1219966.

Hurford, A. J., & Green, P. F. (1983) The zeta age calibration of fission-track dating. Chemical Geology, 41, 285–317. Retrieved from https://www.sciencedirect.com/science/article/abs/pii/S0009254183800266

Inoue A. (1995) Formation of Clay Minerals in Hydrothermal Environments. In *Origin and Mineralogy of Clays* B. Velde (ed.). Springer, Berlin, Heidelberg. pp. 268–329.

Inoue A., Inoué S. and Utada M. (2018) Application of chlorite thermometry to estimation of formation temperature and redox conditions. Clay minerals, 53, 143–158.

Jepson, G., Carrapa, B., George, S. W. M., Triantafyllou, A., Egan, S. M., Constenius, K. N., Gehrels, G. E., & Ducea, M. N. (2021). Resolving mid- to upper-crustal exhumation through apatite petrochronology and thermochronology. Chemical Geology, 565, 120071. https://doi.org/10.1016/j.chemgeo.2021.120071

Jiang W.-T. and Peacor D. R. (1994) Formation of corrensite, chlorite and chlorite-mica stacks by replacement of detrital biotite in low-grade pelitic rocks. Journal of Metamorphic Geology, 12, 867–884.

Keller, W. (1953). Illite and montmorillonite in green sedimentary rocks. Journal of Sedimentary Research, 23, 3–9.

Ketcham, R. A., Carter, A., Donelick, R. A., Barbarand, J., & Hurford, A. J. (2007). Improved modeling of fission-track annealing in apatite. American Mineralogist, 92(5–6), 799. https://doi.org/10.2138/am.2007.2281

Kim J.H., Bailey L., Noyes C., Tyne R.L., Ballentine C.J., Person M., Ma L., Barton M., Barton I., Reiners P.W., Ferguson G., McIntosh J.: Hydrogeochemical evolution of formation waters responsible for sandstone bleaching and ore mineralization in the Paradox Basin, Colorado Plateau, USA (2022) GSA Bulletin, 134(9-10), 2589-2610.

Kluth, C.F., Coney, P.J. (1981). Plate tectonics of the Ancestral Rocky Mountains. Geology, 9 (1): 10–15. doi: https://doi.org/10.1130/0091-76139

Kogel J. E. (2001) Baseline Studies of the Clay Minerals Society Source Clays: Chemical Analysis by Inductively Coupled Plasma-Mass Spectroscopy (ICP-MS). Clays and Clay Minerals, 49, 387–392.

Lanari P., Wagner T. and Vidal O. (2014) A thermodynamic model for di-trioctahedral chlorite from experimental and natural data in the system MgO–FeO–Al2O3–SiO2–H2O: applications to P–T sections and geothermometry. Contributions to Mineralogy and Petrology, 167, 968.

Lang, K. A., Jepson, G., Ye, Z., & Kim, W. (2023). New tools for digital fission-track analysis. *AGU23*.

Laslett, G. M., Kendall, W. S., Gleadow, A. J. W. & Duddy, I. R. (1982) Bias in measurement of fission-track length distributions, Nuclear Tracks and Radiation Measurements 6(2), 79– 85. http://www.sciencedirect.com/science/article/pii/0735245X8290031X

Lawton, T.F., Blakey, R.C., Stockli, D.F., & Liu, L. (2021). Late Paleozoic (Late Mississippian–Middle Permian) sediment provenance and dispersal in western equatorial Pangea. Palaeogeography, Palaeoclimatology, Palaeoecology. 572. 110386. 10.1016/j.palaeo.2021.110386.

Leary, R.J., Umhoefer, P., Smith, M.E., Riggs, N. (2017) A three-sided orogen: A new tectonic model for Ancestral Rocky Mountain uplift and basin development. Geology, 45 (8), 735–738. doi: https://doi.org/10.1130/G39041.1

McBride, E. (1974). Significance of color in red, green, purple, olive, brown, and gray beds of Difunta Group, northeastern Mexico. Journal of Sedimentary Research, 44, 760–773.

McDowell, F. W., McIntosh, W. C., & Farley, K. A. (2005). A precise $^{40}Ar^{39}Ar$ reference age for the Durango apatite (UTh)/He and fission-track dating standard. Chemical Geology, 214(3), 249–263. http://www.sciencedirect.com/science/article/pii/S0009254104004218

Mermut A. R. (2001) Baseline Studies of the Clay Minerals Society Source Clays: Chemical Analyses of Major Elements. Clays and Clay Minerals 49, 381–386.

Meunier A: Clays (2005) Springer Science & Business Media.

Moore, D. M., & Reynolds, Robert C. (1989). *X-ray diffraction and the identification and analysis of clay minerals / Duane M. Moore and Robert C. Reynolds, Jr.* Oxford [England] ; New York: Oxford University Press.

Moore, K., Soreghan, G., and Sweet, D. (2008) Stratigraphic and Structural Relations in the Proximal Cutler Formation of the Paradox Basin: Implications for Timing of Movement on the Uncompahgre Front. Mountain Geologist, 45, 49-68.

Morrison, S. J. and Parry, W.T. (1986). Dioctahedral corrensite from Permian Red Beds, Lisbon Valley, Utah. Clays and Clay Minerals, 34(6), 613–624. https://doi.org/10.1346/ccmn.1986.0340601

Murakami, T., Ito, J., Utsunomiya, S., Kasama, T., Kozai, N., & Ohnuki, T. (2004) Anoxic dissolution processes of biotite: implications for Fe behavior during Archean weathering. Earth and Planetary Science Letters**,** 224, 117-129.

Murray, K.E., Reiners, P.W., and Thomson, S.N. (2016) Rapid Pliocene–Pleistocene erosion of the central Colorado Plateau documented by apatite thermochronology from the Henry Mountains: Geology, v. 44, p. 483–486, doi:10.1130/G37733.1.

Murray, K.E., Reiners, P.W., Thomson, S.N., Robert, X., and Whipple, K.X. (2019) The thermochronologic record of erosion and magmatism in the Canyonlands region of the Colorado Plateau: American Journal of Science, 319, 339–380, https://doi.org/10 .2475/05.2019.01

Naeser, C., Bryant, B., Kunk, M. J., Kellogg, K. S., Donelick, R. and Perry Jr, W. (2002) Tertiary cooling and tectonic history of the White River uplift, Gore Range, and western Front Range, central Colorado: Evidence from fission-track and 39Ar/40Ar ages. GSA Special Papers 366, 31 – 53. doi: 10.1130/0-8137-2366-3.31

Nuccio, V.F., and Condon, S.M. (1996) Burial and thermal history of the Paradox Basin, Utah and Colorado, and petroleum potential of the Middle Pennsylvanian Paradox Formation: U.S. Geological Survey Bulletin 2000-O, 41 p., https://doi.org/10.3133/b00O.

Pant S., Singh S., Sahoo P. R., Kumar A., Saravanan B., Venkatesh A. S., Yadav G. S. and Kumar P. (2019) Mineral chemistry and geothermometry of chlorites in relation to physico-chemical conditions of uranium mineralization in the central part of the Singhbhum Shear Zone, eastern India. *Ore Geology Reviews* **112**, 102997.

Parneix J. C., Beaufort D., Dudoignon P. and Meunier A. (1985) Biotite chloritization process in hydrothermally altered granites. Chemical Geology 51, 89–101.

Reiners, P. W. (2005) Zircon (U-Th)/He thermochronometry. In Reviews in mineralogy and geochemistry (Vol. 58, pp. 151–179). https://doi.org/10.2138/rmg.2005.58.6

Reynolds, R.C. Jr. (1988) Mixed layer chlorite minerals. In Mineralogical Society of America Reviews in Mineralogy, 19, 601–629.

Reynolds R.L., Hudson M.R., Fishman N.S., Campbell J.A. (1985) Paleomagnetic and petrologic evidence bearing on the age and origin of uranium deposits in the Permian Cutler Formation, Lisbon Valley, Utah. GSA Bulletin, 96(6), 719-730.

Rønnevik, C., Ksienzyk, A.K., Fossen, H., & Jacobs, J. (2017) Thermal evolution and exhumation history of the Uncompahgre Plateau (northeastern Colorado Plateau), based on apatite fission track and (U-Th)-He thermochronology and zircon U-Pb dating. Geosphere, 13(2), 518–537. https://doi.org/10.1130/ges01415.1

Soreghan G.S., Sweet D.E., Marra K.R., Eble C.F., Soreghan M.J., Elmore R.D., Kaplan S.A., Blum M.D.: An exhumed late Paleozoic canyon in the Rocky Mountains (2007) Journal of Geology, 115(4), 473-481.

Soreghan G.S., Soreghan M.J., Sweet D.E., Moore K.D.: Hot fan or cold outwash? Hypothesized proglacial deposition in the upper Paleozoic Cutler Formation, western tropical Pangea (2009) Journal of Sedimentary Research,79(7), 495-522.

Soreghan, G. S., Sweet, D. E., & Heavens, N. G. (2014). Upland glaciation in Tropical Pangaea: Geologic evidence and implications for late Paleozoic climate modeling. The Journal of Geology, 122(2), 137–163. https://doi.org/10.1086/675255

Soreghan G.S., Sweet D.E., Thomson S.N., Kaplan S.A., Marra K.R., Balco G., Eccles T.M.: Geology of Unaweep Canyon and its role in the drainage evolution of the northern Colorado Plateau (2015b) Geosphere, 11(2), 320-341.

Środoń J: Nature of mixed-layer clays and mechanisms of their formation and alteration (1999) Annual Reviews in Earth and Planetary Science, 27, 19–53.

Sugimori H., Iwatsuki T. and Murakami T. (2008) Chlorite and biotite weathering, Fe^{2+}-rich corrensite formation, and Fe behavior under low PO_2 conditions and their implication for Precambrian weathering. American Mineralogist, 93, 1080–1089.

Suttner, L.J., Dutta, P.K. (1986) Alluvial sandstone composition and paleoclimate, I. Framework Mineralogy. SEPM Journal of Sedimentary Research, Vol. 56. https://doi.org/10.1306/212f8909-2b24-11d7-8648000102c1865d

Sweet, D. and Soreghan, G. (2010) Late Paleozoic tectonics and paleogeography of the ancestral Front Range: Structural, stratigraphic, and sedimentologic evidence from the Fountain Formation (Manitou Springs, Colorado). Geological Society of America Bulletin. 122. 575-594. 10.1130/B26554.1.

Van Houten, F. B. (1973) Origin of Red Beds - Review, 1961-1972. Annual Review of Earth and Planetary Sciences, 1, 39–61.

Vermeesch, P. (2009) RadialPlotter: a Java application for fission track, luminescence and other radial plots, Radiation Measurements, 44, 4, 409-410

Vermeesch, P. (2017) Statistics for LA-ICP-MS based fission track dating, Chemical Geology, 456, 1927. URL: http://www.sciencedirect.com/science/article/pii/S0009254117301158

Werner, W.G. (1974) Petrology of the Cutler Formation (Pennsylvanian-Permian) near Gateway, Colorado, and Fisher Towers, Utah. SEPM Journal of Sedimentary Research, 44(2), 292-298. https://doi.org/10.1306/74d72a18-2b21-11d7-8648000102c1865d

White, M.A. and Jacobson, M.I. (1983) Structures associated with the southwest margin of the ancestral Uncompahgre Uplift; *in* W.R. Averett, ed., Northern Paradox Basin-Uncompahgre Uplift: Grand Junction Geol.Soc., Grand Junction, CO, p.33-39.

Wu, D., Jiayong, P., Fei, X., Guangwen, H., and Jing, L. (2019) The Mineral Chemistry of Chlorites and Its Relationship with Uranium Mineralization from Huangsha Uranium Mining Area in the Middle Nanling Range, SE China, *Minerals* 9(3), 199. https://doi.org/10.3390/min9030199